INTERNAL RESISTANCE AS TERMINATION INDICATOR DURING LEAD-ACID BATTERY FORMATION

by

Christopher White

Submitted in partial fulfilment of the requirements
for the degree of Master of Applied Science

at

Dalhousie University
Halifax, Nova Scotia
August 2015

Table of Contents

List of Tables

List of Figures

Abstract

Lead-acid batteries are a reliable, inexpensive energy storage technology used extensively in a wide range of applications. Before selling this technology to customers however, manufacturers must subject the batteries to a time- and energy-intensive charge known as formation. As more capacity is charged into the batteries during formation, more capacity will be available for discharge by the customer. Since the output per unit input has diminishing returns, knowing when best to terminate a formation is of economic importance to manufacturers. In this study, internal battery resistance is introduced as a novel termination indicator. Resistance trends are first measured during a series of laboratory-based formations. The trends are then correlated with formation completeness such that a manufacturer would be able to identify a suitable termination point based on these non-invasive in situ measurements. The method is partially verified for large-scale battery production through additional experimentation in a lead-acid battery manufacturing facility.

List of Abbreviations and Symbols Used

Acronyms

AC	Alternating current
DC	Direct current
EDL	Electrochemical double-layer
EMF	Electromotive force
LAB	Lead-acid battery
NAM	Negative active mass
NEP	Negative electrode potential
PAM	Positive active mass
PEP	Positive electrode potential
pH	Power of hydrogen
SOC	State of charge
SBCL	Surrette Battery Company Limited
SG	Specific gravity
TC	Theoretical capacity
VRLA	Valve-regulated lead-acid

Symbols

a	Chemical activity
A	Area (m^2)
C	Capacitance (F)
C_{dl}	Double-layer capacitance (F)
Cap	Electric capacity (Ah)
Cap_r	Electric capacity corrected to a reference temperature (Ah)
d	Distance (m)
DR	Differential resistance (Ω)
E	Electrical potential or voltage (V)
E^0	Standard potential of an electrode (V)
E_{eq}	Equilibrium potential of an electrode (V)
F	Faraday constant ($96485.3365\ldots\ C \cdot mol^{-1}$)
i_0	Exchange current density ($A \cdot m^{-2}$)
I	Electrical current (A)
IR	Battery internal electrical resistance (Ω)
n	Number of electrons transferred in an electrochemical reaction
R	Universal gas constant ($8.314\ldots\ J \cdot mol^{-1} \cdot K^{-1}$)
R_{ct}	Charge-transfer resistance (Ω)
R_o	Ohmic resistance (Ω)
s	Stoichiometric coefficient
T	Temperature (K or °C)
T_1	Initial discharge temperature (°C)
Tr	Reference temperature (°C)
u	Uncertainty
Z	Electrical impedance (Ω)
Z_W	Warburg impedance (Ω)

Greek Letters

α	Charge-transfer coefficient
ε_0	Electrical permittivity of a vacuum ($8.854\ldots \times 10^{-12}$ $F \cdot m^{-1}$)
ε_1	Relative electrical permittivity ($F \cdot m^{-1}$)
η	Activation overpotential (V)
θ	Phase angle
λ	Discharge capacity temperature-correction constant (K^{-1})

Subscripts

Im	Imaginary
N	Negative
O	Oxidation
P	Positive
R	Reduction
Re	Real

Chemical Nomenclature

H	Hydrogen
Hg	Mercury
O	Oxygen
Pb	Lead
S	Sulfur

Acknowledgements

First and foremost, I want to extend my deepest thanks to my supervisor, Dr. Lukas Swan. It has been a pleasure and a privilege to have spent these past years working with such a brilliant, fun, and supportive person. He has made countless efforts to improve me as an engineer, and I have no doubt that the experiences he has given me will continue to benefit me far into the future. His relentless optimism and genuine interest in his students are the foundation of this thesis, and I hope that my efforts adequately reflect my gratitude.

I would also like to thank my supervisory committee members, Dr. Dominic Groulx and Dr. Adam Donaldson. Their recommendations throughout this project have been truly valuable, and their enthusiastic participation is sincerely appreciated. The entire faculty and staff of the Dalhousie University Department of Mechanical Engineering must be thanked as well, for all they have done to make my success possible.

The entire research team at the Renewable Energy Storage Laboratory deserves thanks for their support and their friendship throughout my studies. In particular, I must recognize my partner-in-crime, Justin Deveau. We have shared a roller coaster car for the last two years, and he has been a phenomenal teammate and friend throughout the journey. I am thrilled that we have made it to the end of the ride together.

I would also like to thank Pascal Ferron and the rest of the team at Surrette Battery Company, whose contributions made this project possible. A special thanks also goes to the Natural Sciences and Engineering Research Council of Canada for supporting our research, and to Dr. Robert Gillespie for his generous financial donations to a long list of grateful Dalhousie graduate students.

Finally, I want to thank my family and friends for the never-ending love and support that has always kept me going.

Chapter 1   Introduction

This thesis develops a novel technique for determining when an important stage (called 'formation') in the lead-acid battery manufacturing process is complete. The technique is based on measuring the internal resistance of the battery throughout formation, as a means of non-invasively monitoring the changing electrochemistry inside the battery. The project includes extensive experimentation both in a laboratory setting and in an industrial setting, with supportive explanations of the observed results through electrochemical theory.

1.1.   Project Background

The lead-acid battery (LAB) is an electrochemical energy storage technology commonly used in systems all over the world, including backup power, electric vehicles, ignition systems, and renewable energy. The manufacturing process of these batteries involves an energy-intensive step known as 'formation', which electrochemically activates the batteries through a long electrical charge. The amount of formation capacity applied to the batteries determines how much discharging capacity will be available to the customer upon delivery and during subsequent cycling, where additional formation input provides diminishing additional available discharge output. When the storage application is grid-connected, the customer is able to fully charge the battery as necessary and complete the formation, such that the manufacturer can "under-form" in the factory in order to reduce costs and production time. In contrast, batteries in off-grid applications rarely receive a full charge and completing the formation during operation is unlikely. Therefore, manufacturers should fully form off-grid batteries before they leave the factory in order to ensure the initial performance meets the customers' expectations. Having the ability to detect completeness of formation is therefore of value to a LAB manufacturer, so as to deliver the highest performance product without wasting unnecessary energy and time for manufacture.

Presently, manufacturers form LABs according to a generalized algorithm, which is based mainly on the size of the battery and does not take the end-use application into account. The best non-invasive method for confirming that the algorithm has successfully formed the battery to the desired level is to deep discharge cycle the battery and determine if the

resulting output capacity meets specifications. However, this requires sampling batteries from every batch for testing and the test itself requires additional advanced testing equipment. Alternatively, invasive techniques can determine formation completeness by disassembling the formed battery and visually inspecting the electrodes, or by performing a more advanced chemical analysis to determine the exact electrode composition.

The LAB industry could benefit from a non-invasive method for monitoring the completeness of formation in situ. If a LAB manufacturer had access to such a method, they would be able to make any of the following determinations regarding their formation strategies:

1. Existing strategies are not forming a given battery to an acceptable level and should therefore provide additional formation capacity in the factory in order to satisfy customer expectations.

2. Existing strategies are forming a given battery more than necessary and should therefore reduce formation capacity in the factory in order to save energy and time of manufacture.

3. New or experimental battery models can be formed optimally for a given application without conducting additional tests or assuming existing generalized algorithms can be applied.

Manufacturers of formation chargers can also benefit from the development of an in situ method for monitoring formation progress. Such a method could be implemented into their formation charger software features, displaying live trends on a monitor in a battery manufacturing plant. The appropriate termination point could then be determined automatically by the formation software or manually by the judgement of a trained operator.

This thesis explores battery internal resistance as a potential indicator of formation completeness. During the formation of a LAB, electrochemically inactive materials in the electrodes are converted into electrochemically active ones. This means that in general, as the battery undergoes formation its electrical conductivity improves, and the

electrochemical reaction kinetics evolve with the changing electrode composition. The electrical conductivity and reaction kinetics determine the internal resistance of the battery, so it follows then that the trending resistance may display unique characteristics when the formation is complete. These resistance trends can be measured at any point during a formation by superimposing electrical current transients over the constant formation current and measuring the corresponding electrical voltage response, as per Ohm's law. This thesis project aims to employ such methods, with the hypothesis that the measured internal resistance trends can provide LAB manufacturers with a way to non-invasively monitor formation progress in situ and detect when the formation is complete.

1.2. Project Objectives

The identified hypothesis can only be properly tested through experimental work, although a thorough understanding of electrochemical theory is also necessary for the design of experiments and interpretation of results. Experimentation requires unformed LABs and advanced equipment capable of forming them while measuring their internal resistance. Experiments must be conducted in a controlled laboratory environment in order to obtain accurate results, but even successful laboratory experiments will not necessarily be scalable to mass production in a LAB manufacturing plant. The observed results must also be repeatable regardless of the parameters of formation (e.g. current, voltage, temperature, battery size, etc.). With all of these things in mind, the following project objectives were identified:

1. Develop a battery resistance measurement strategy that can be employed in situ during LAB formation.
2. Successfully form LABs in a laboratory setting using the developed resistance measurement strategy.
3. Validate the observed resistance trends through electrochemical theory.
4. Develop a method for identifying the appropriate termination point during formation based on in situ resistance trends.
5. Successfully employ the developed method in various laboratory formation conditions.
6. Successfully employ the developed methods in an actual LAB manufacturing plant.

Chapter 2   Relevant Theory and State-of-the-Art

This chapter will provide the necessary theoretical background surrounding LABs, internal resistance, and formation. Findings from related existing research will be cited throughout in order to identify the current state-of-the-art and the research gaps of interest to this project.

2.1.   Introduction to Lead-acid Batteries

Figure 1 and Figure 2 illustrate the main components of a LAB as well as the reactions that occur at each electrode during discharge and charge. The cell is composed of a positive electrode and a negative electrode which are immersed in an aqueous electrolyte of sulfuric acid (H_2SO_4). As a diprotic acid, the electrolyte dissociates into sulfate ions (SO_4^{2-}), hydrogen sulfate ions (HSO_4^-), and hydrogen ions (H^+). The flow of electrons are carried to/from each electrode through the current collector grid to an external circuit, and the internal circuit is completed by ionic charge flows through the electrolyte. In the diagrams, the blue flows represent the current from electron flow, while the green flow represents the current from H^+ ion flow. The value of I represents the magnitude of the electrical current flows, which must be equivalent for a complete circuit. The black flows and red boxes identify the reaction processes. Note that if the positive and negative electrodes come into physical contact with each other while immersed in the electrolyte it will cause an electrical short. This is prevented through use of a porous separator membrane which is electrically insulating but permeable to ionic current.

At the fully charged state, the negative electrode contains sponge lead (Pb) and the positive electrode contains lead dioxide (PbO_2), while at the fully discharged state both electrodes contain lead sulfate ($PbSO_4$). The overall reversible reaction at the positive electrode can be described as:

$$(\textbf{charged}) \quad PbO_2 + SO_4^{2-} + 4H^+ + 2e^- \leftrightarrow PbSO_4 + 2H_2O \;\; (\textbf{discharged}) \qquad (1)$$

and at the negative electrode:

$$(\textbf{charged}) \quad Pb + SO_4^{2-} \leftrightarrow PbSO_4 + 2e^- \;\; (\textbf{discharged}) \qquad (2)$$
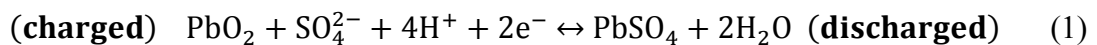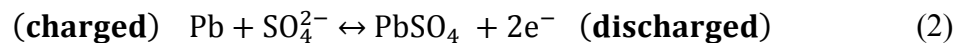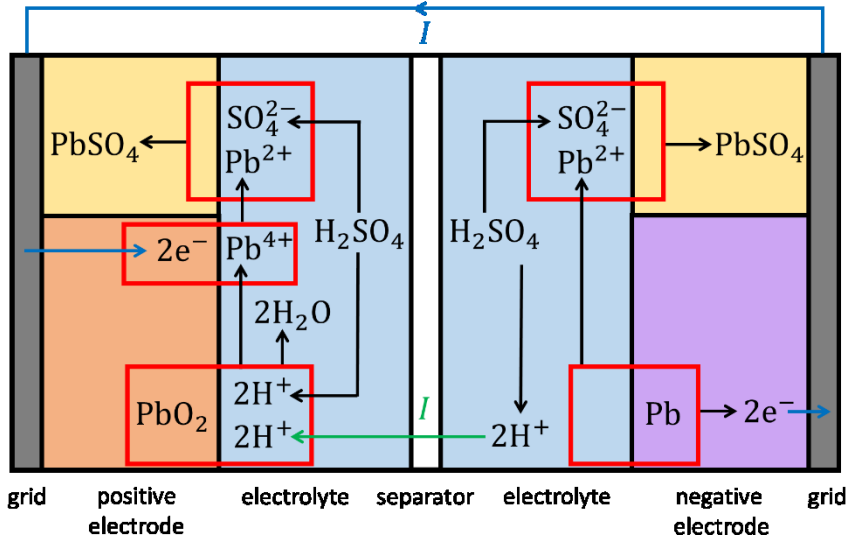
Figure 1   Discharge reactions of a LAB
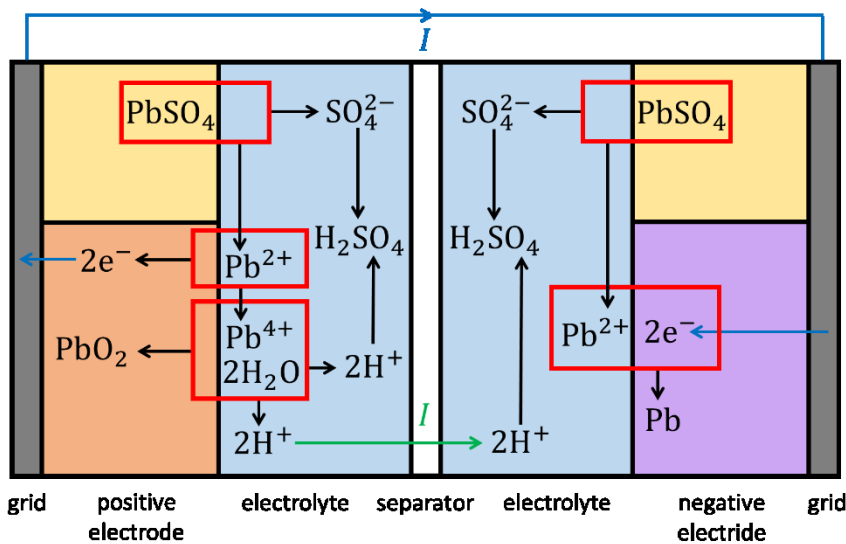
Figure 2   Charge reactions of a LAB

During discharge, electrons are released from the negative electrode and flow through an external circuit, to be accepted by the positive electrode. At the same time, SO_4^{2-} anions are taken out of the electrolyte at the negative electrode, leaving a high concentration of H^+ cations. Meanwhile at the positive electrode, four H^+ cations $(+4)$ are removed from the electrolyte for every one SO_4^{2-} anion removed (-2), resulting in a low concentration of H^+ cations at the positive electrode. The electric field generated inside the cell as well as the concentration gradient between the two electrodes cause the H^+ cations to migrate/diffuse from the negative electrode through the separator to the positive electrode.

This mechanism completes the circuit and balances the charge distribution in the electrolyte. The reverse mechanism will occur on charge as electrons and H^+ cations flow from the positive electrode to the negative electrode. It can be seen in Figure 1 and Figure 2 that the actual electron-transfer step always involves a lead (II) ion (Pb^{2+}).

The reaction mechanisms in Eq. (1) and Eq. (2) also show how the H^+ and SO_4^{2-} ions in the electrolyte are consumed by the electrodes during discharge and released back into the electrolyte during charge. It can therefore be inferred that the electrolyte concentration will decrease as the cell is discharged and increase as it is charged. This feature of LABs allows for electrolyte specific gravity (SG) measurements to be used as an indicator of the state-of-charge (SOC) of the cell.

It is important to note that 'formation' is essentially the first charge of the battery, but as the electrodes are not built of PbSO4 by the manufacturer, additional processes take place during formation. These processes will be discussed in section 2.6.

2.2.   Equilibrium Conditions

When there are no net charge transfer processes occurring a cell can be considered to be in equilibrium, and every electrode system has an equilibrium potential (relative to some reference potential) that is specific to its electrochemistry. The equilibrium potential is described by the Nernst equation [1]:

$$E_{eq} = E^0 + \frac{RT}{nF} \ln \left(\prod_i (a_i)^{s_i} \right)$$ (3)

For reactions of the form:

$$\text{Oxidation products} + n\text{e}^- \leftrightarrow \text{Reduction products}$$ (4)
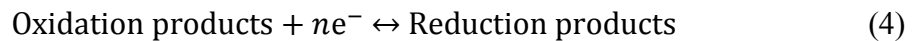
where

E_{eq} is the equilibrium potential of the electrode, in V

E^0 is the standard potential of the electrode, in V

R is the universal gas constant, $8.314\ldots\ \text{J} \cdot \text{mol}^{-1} \cdot \text{K}^{-1}$

T is the temperature, in K

n is the number of electrons transferred in the reaction (equal to 2 for LABs)

F is the Faraday constant, $96485.3365\ldots$ $C \cdot mol^{-1}$

a_i is the activity (approximately the concentration) of a given species in the reaction

s_i is the stoichiometric coefficient of a given reactions species (negative for reduction products)

E^0 is then defined as the electrode potential when the activity of oxidized products and reduced products are the same. Since the activity of solids is equal to 1 [1], the equilibrium potential at standard conditions for the negative electrode (relative to the standard hydrogen electrode) is:

$$\left(E_{eq}\right)_N = -0.358 + 0.0000992T \log_{10}\left((a_{SO_4^{2-}})^{-1}\right)$$
$$= -0.358 - 0.0000992T \log_{10}\left(a_{SO_4^{2-}}\right) \tag{5}$$

while that of the positive electrode is:

$$\left(E_{eq}\right)_P = 1.683 + 0.0000992T \log_{10}\left((a_{SO_4^{2-}})^1 (a_{H^+})^4 (a_{H_2O})^{-2}\right)$$
$$= 1.683 + 0.0000992T \log_{10}\left(a_{SO_4^{2-}}\right) - 0.00397T\text{pH} \tag{6}$$
$$- 0.000198T \log_{10}\left(a_{H_2O}\right)$$

Note that the negative of the decimal logarithm of H^+ ion activity is the definition of the power of hydrogen (pH). In turn, the electromotive force (EMF) of a full electrochemical cell is the difference between the equilibrium potential of the positive electrode and that of the negative electrode. The EMF in volts of a LAB is therefore defined as:

$$EMF = \left(E_{eq}\right)_P - \left(E_{eq}\right)_N$$
$$= 2.041 - 0.00397T\text{pH} + 0.000198T \log_{10}\left(a_{SO_4^{2-}}\right) \tag{7}$$
$$- 0.000198T \log_{10}\left(a_{H_2O}\right)$$

Thus the EMF of a single-cell LAB is nominally 2.041 V at standard conditions, which decreases with pH and water activity and increases with sulfate activity. The three variable terms of Eq. (7) can be considered qualitatively as one effect by combining them as follows:

$$EMF = 2.041 + 0.000198 \log_{10}\left(\frac{a_{H_2SO_4}}{a_{H_2O}}\right) T \tag{8}$$

Now it can be clearly seen that a higher electrolyte concentration (which is an indicator of high SOC) will result in an increased EMF, and a lower electrolyte concentration (which is an indicator of low SOC) will result in a decreased EMF. This means that measuring the EMF of a LAB in equilibrium can give an indication of the SOC, similarly to measuring the electrolyte SG. Note that at "standard conditions", the electrolyte molarity is defined at 1 M (1.06 kg/L), which is only found in practice in a fully discharged LAB. A fully charged LAB will have an EMF between 2.10 and 2.15 V per cell [2]. Eq. (8) also shows that the EMF will increase linearly with temperature when all other variables are held constant.

2.3. Non-equilibrium Conditions

In order for the cell to charge or discharge, the electrode-electrode system must move away from equilibrium. For discharge, the positive and negative electrodes of the cell must be connected through a load, allowing a limited current of electrons to flow from the negative to the positive. For charge, current must be forced such that electrons flow from the positive to the negative. These non-equilibrium conditions involve voltage drops inside the cell that will lower the cell voltage on discharge and raise the cell voltage on charge. These voltage drops include ohmic losses, activation overpotential, and mass transport effects, which are described in more detail in the following subsections.

2.3.1. Ohmic Losses

Ohmic losses are voltage drops that occur strictly due to Ohm's law, which states that the voltage drop across a resistive element will be directly proportional to the magnitude of the current flowing through it. All of the metallic components in a LAB will have some resistance to electron flow, including the current collectors, as well as the electrode materials themselves, which must conduct electrons to the reaction site at the electrode-electrolyte interface. While the grid, welds, and tabs will have a fixed electrical resistance for a given battery (barring large temperature fluctuations or corrosion with age), the resistance of the electrode materials will be a function of a battery's state of charge, as well as its state of formation. Prior to formation, the electrode materials consist of a paste of lead oxide (PbO) and basic lead sulfates, which are poor conductors. During formation, these poor conductors are converted to PbO_2 at the positive electrode and Pb at the negative electrode, which are much better conductors (formation processes are described in greater

detail in section 2.6). During discharge, the electrode materials are converted back to $PbSO_4$, which is reversed on recharge. Table 1 compares the approximate specific resistivity values of the main components of the electrode materials.

Table 1   Specific resistivity of electrode materials

Name	Description	Specific resistivity (Ω cm)
PbO	Unformed paste	~10^{12} [3]
$PbSO_4$	Partially formed paste and discharged electrodes	0.3×10^{10} [4]
PbO_2	Formed/charged positive electrode	2×10^{-4} [4]
Pb	Formed/charged negative electrode	0.2×10^{-4} [4]

While the metals have an electronic resistance, the electrolyte has an ionic resistance that will contribute to the overall ohmic losses. The ionic resistance of H_2SO_4 is a function of both concentration and temperature. Highly concentrated acid will have low ionization and therefore high resistance, so increasing the water content increases the number of ions and thus decreases the resistance. However, once the maximum ionization has been achieved, additional water will reduce the overall ion concentration and thus increase the resistance. This means that a minimum resistance exists. For H_2SO_4, there is a broad valley between SGs of 1.100 and 1.280 where the specific resistance lies between 1.2 Ω cm and 1.7 Ω cm at 25 °C, outside of which the resistance increases relatively sharply [2]. For this reason, LABs are typically designed to operate in this SG range, where 1.100 would represent a fully discharged state and 1.280 a fully charged state. In contrast, the temperature dependence is unidirectional. Higher temperatures allow for faster ion movement, which corresponds to lower ionic resistance.

Since ions must move through the pores of the separator through migration and diffusion, the separator will also contribute to the ionic resistance. The ionic resistance of the separator will decrease with higher porosity and increase with higher tortuosity factor, which is a measure of the ionic mean path length through the membrane relative to the actual thickness of the membrane [5]. Since these two properties are fixed for a given separator, its ionic resistance will not change with SOC.

2.3.2.   Activation Overpotential

The activation overpotential is the extra potential above or below the equilibrium potential that is required to drive the electrochemical reactions in order to achieve a certain current.

The faradaic current (electrical current obtained through electrochemical reaction) obtained from a given overpotential is described by the Butler-Volmer equation [6]:

$$I = i_0 A \left[e^{\alpha_O \frac{nF}{RT} \eta} - e^{-\alpha_R \frac{nF}{RT} \eta} \right] \tag{9}$$

where

I is the faradaic current into or out of the electrode in question, in A

i_0 is the exchange current density at the electrode, in $A \cdot m^{-2}$

A is the area of the reaction surface, in m^2

$\alpha_O + \alpha_R = 1$ defines the charge transfer coefficients of oxidation and reduction processes

η is the activation overpotential ($\eta = E - E_{eq}$), in V

The exchange current represents the rate at which oxidation and reduction proceed in equilibrium with no net current. It is itself a function of temperature, reactant concentration, and the electrode system in question [6]. Eq. (9) also illustrates how a larger overpotential is required to obtain the same current when the reacting surface area of the electrode is smaller. This influence is manifested in practice when electrode dimensions limit current capability and also when the remaining active area available for reaction in a given electrode changes as it is discharged or charged. The main point to take away from Eq. (9) is that charge-transfer increases exponentially with overpotential.

Typically when Eq. (9) is plotted it shows the net current I as well the individual terms representing oxidation current and reduction current, as done in Figure 3. The plot illustrates how current is always flowing in both directions as an exponential function of overpotential. The higher the overpotential in one direction, the more that current direction is favored over the other.
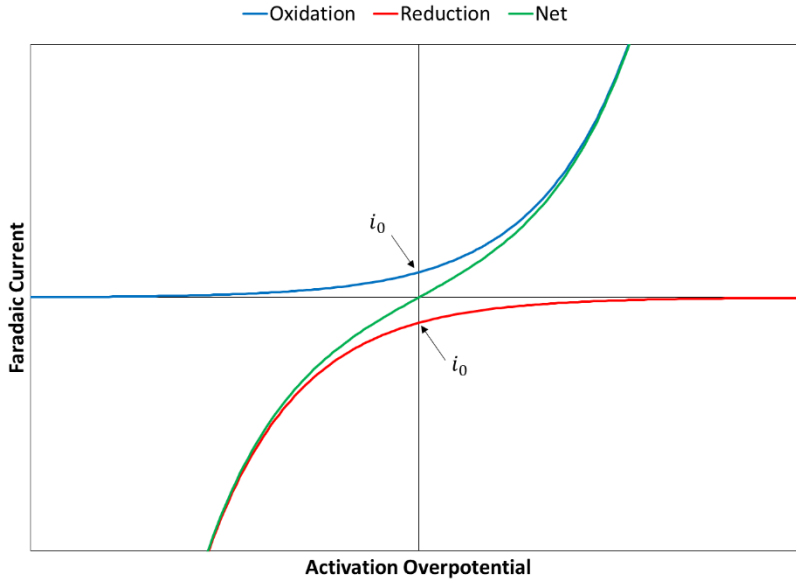
Figure 3   Typical graphical representation of the Butler-Volmer equation

From Figure 3 , it can be seen that attempting to increase the current by a factor of 2 would require an increase in overpotential by a factor of < 2, and increasing the current by a factor of 100 would require an increase in overpotential of $<< 100$. This relationship describes the charge-transfer resistance, R_{ct}:

$$R_{ct} = \frac{\eta}{I} = \frac{\eta}{i_0 A}\left[e^{\alpha_O \frac{nF}{RT}\eta} - e^{-\alpha_R \frac{nF}{RT}\eta}\right]^{-1} \tag{10}$$

Figure 4 shows how R_{ct} decreases at higher activation overpotentials according to Eq. (10). Also note that the area, A, in the denominator indicates that reduction in the reacting surface area of the electrode will cause R_{ct} to increase.
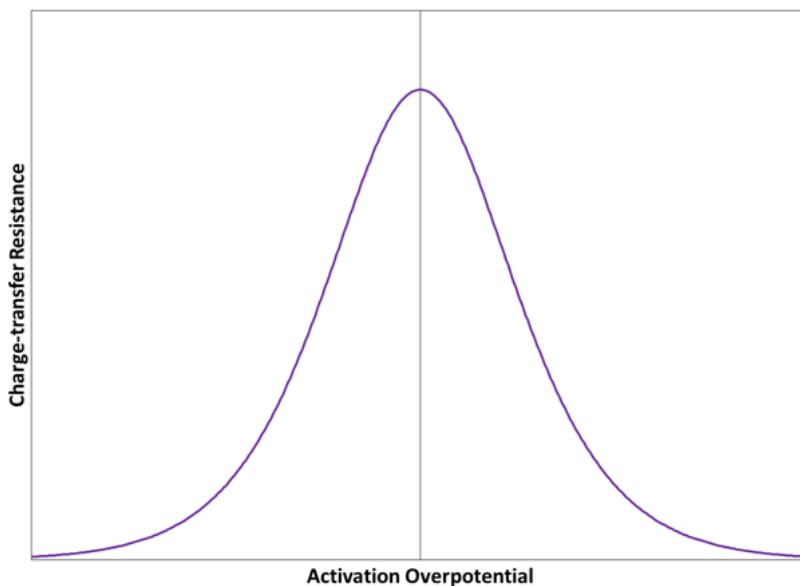
Figure 4   Charge-transfer resistance as a function of overpotential

2.3.3.   Mass Transport Effects

At relatively low currents, ionic transport through the electrolyte allows reactants and products at the electrode-electrolyte interface to be replaced as quickly as they are consumed or to be removed as quickly as they are released from the electrode, and an even distribution of ions is maintained throughout the electrolyte. However, if the current is high enough, limited mass transport will give rise to concentration gradients in the electrolyte, causing the effective concentration seen by the electrode to be different from the bulk electrolyte concentration.

Three voltages have been discussed thus far – equilibrium potentials, ohmic losses, and activation overpotentials – and all three will be influenced by mass transport effects. Firstly, it was established using the Nernst equation in section 2.2 that the equilibrium potentials of the electrodes are dependent on the concentrations of the reacting species. If the concentrations at the surface of the electrode are skewed by a gradient, then the equilibrium potential is effectively higher or lower than it would be if the gradient did not exist. Second, it was mentioned in subsection 2.3.1 that the ionic resistance of the electrolyte is a function of concentration, and will thus be influenced by gradients as well. Finally, the exchange current used in the Butler-Volmer equation was also stated to be dependent on concentration, so the activation overpotential of the faradaic reactions will

also be affected by mass transport. This essentially means that if there are not enough dissolved reactants at the electrode surface, the activation overpotential must increase to sustain the required current. Overall, mass-transport limitations can cause undesirably low voltages on discharge and high voltages on charge. During operation, this will cause the battery to reach set voltage limits sooner than expected, thereby reducing its performance.

2.4. Electrochemical Double-layer

When an electrode is immersed in an electrolyte, a phenomenon occurs where the surface charge of the electrode attracts ions of the opposite charge (counterions) in the electrolyte, which then approach the surface of the electrode [7]. The counterions are solvated by solvent molecules (water in an aqueous electrolyte), and the finite size of these solvent molecules prevents the counterions from coming into direct contact with the electrode. Thus, a charge separation exists across a dielectric of a thickness on the nanometer scale, and this structure is known as an electric double-layer. When faradaic charge-transfer occurs across this double-layer (as is the case in a battery), it is termed an electrochemical double-layer (EDL). The EDL can charge and discharge electrostatically as the surface charge of the electrode changes, making it analogous to a capacitor with a capacitance defined as:

$$C = \varepsilon_1 \varepsilon_0 \frac{A}{d} \tag{11}$$

where

C is the capacitance, in F

ε_1 is the relative electrical permittivity of the dielectric separating the charges

ε_0 is the electrical permittivity of a vacuum, $8.854\ldots \times 10^{-12}$ F$\cdot$m^{-1}

A is the total surface area of charge separation, in m^2

d is the distance of charge separation, in m

The nanoscale of charge separation in the EDL makes d very small, and in porous membranes such as a battery electrode A will be very high. As a result, EDL capacitance is typically on the orders of farads to hundreds of farads [8].

Apart from ohmic losses, any measured voltage across the terminals of a battery is a combined measurement of the voltages across the EDLs of the positive and negative

electrodes. The equilibrium potential of an electrode can be thought of as the equilibrium charge separation across its EDL. Discharging the electrode reduces the charge separation, and charging increases the charge separation.

Figure 5 illustrates how the EDL potential (red) and ohmic losses (blue) contribute to the measured voltage of a battery. In the diagrams, I represents electrical current from *positive* charge flow. At equilibrium, no current flows, so the ohmic losses are equal to zero and the potentials across the EDLs make up the EMF of the cell (2.041 V at standard conditions, as given in section 2.2). During discharge, the electrodes are depolarized and the EDL potentials are diminished. The current flow further reduces the cell voltage to E_d through ohmic losses in the electrodes and electrolyte. The opposite takes place during charge, where the electrodes are polarized and the ohmic losses further increase the cell voltage to E_c. Thus it becomes clear that the activation overpotential discussed in subsection 2.3.2 is in fact the increase or decrease from the equilibrium potential across the EDL, and this overpotential drives the electrochemical reactions that take place at the EDL itself. Note that the exact structure and mechanisms of the EDL are highly complex, and are discussed in more detail by [9], [10].
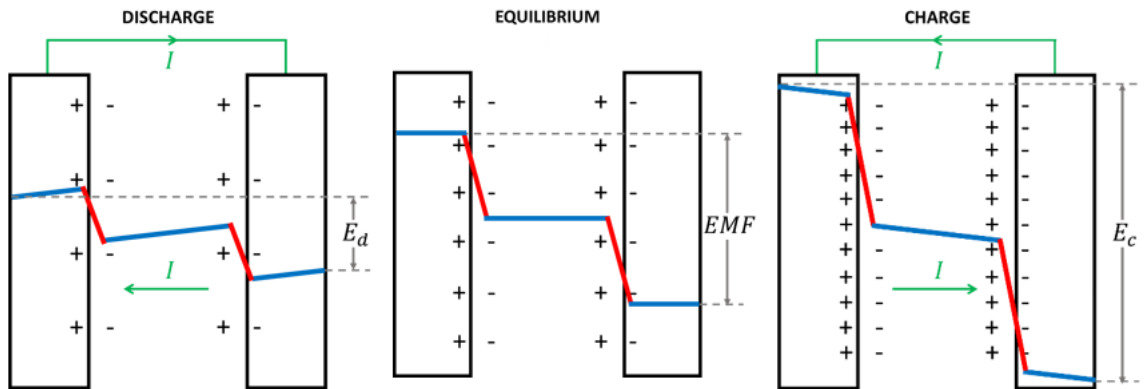
Figure 5   EDL overpotential and ohmic losses in a cell

The capacitance of the EDL describes the relationship between a changing charge separation and the corresponding change in EDL overpotential. When, for example, a load/source is applied, the charges take time to accumulate at the EDL and thus the increase of the EDL overpotential takes time to establish. Thus the rate of change of the EDL charge separation is analogous to the current charging or discharging a capacitor (non-faradaic

current). This effect can cause transients in battery voltage that can last on the order of seconds [7]. As the EDL overpotential increases with time, the faradaic current through the EDL will also increase according to the Butler-Volmer equation (exponentially fast). The sum of the non-faradaic current and faradaic current will equal the total current being passed through the cell. Once the EDL overpotential has reached a steady state, the faradaic current will make up all of the total current.

When the external load/source is removed there is still enough overpotential across the EDL to drive faradaic reactions, but as there is no external current flow to replace the transferred charges, the EDL overpotential decreases over time. This means that there can still be reactions taking place even when a cell is at open circuit, which draws a distinction between 'open circuit' and 'equilibrium'.

2.5. Electrolysis Side Reactions

As with most batteries, LABs will undergo side reactions above a certain overpotential threshold. While there are a number of these reactions, the most significant by far is water electrolysis [1]. Figure 6 illustrates the basic mechanisms of electrolysis at the positive and negative electrodes during charge. As in Figure 1and Figure 2, black flows and red boxes indicate reaction processes, while blue flows indicate electronic current and green flows represent ionic current. At the positive electrode, water is oxidized to produce oxygen gas (O_2) and an excess of H^+ ions, while at the negative electrode, H^+ ions are reduced to produce hydrogen gas (H_2). The migration/diffusion of H^+ ions from the positive electrode to the negative electrode corrects the charge imbalance and completes the circuit, as it does during the main charging reaction (see section 2.1).
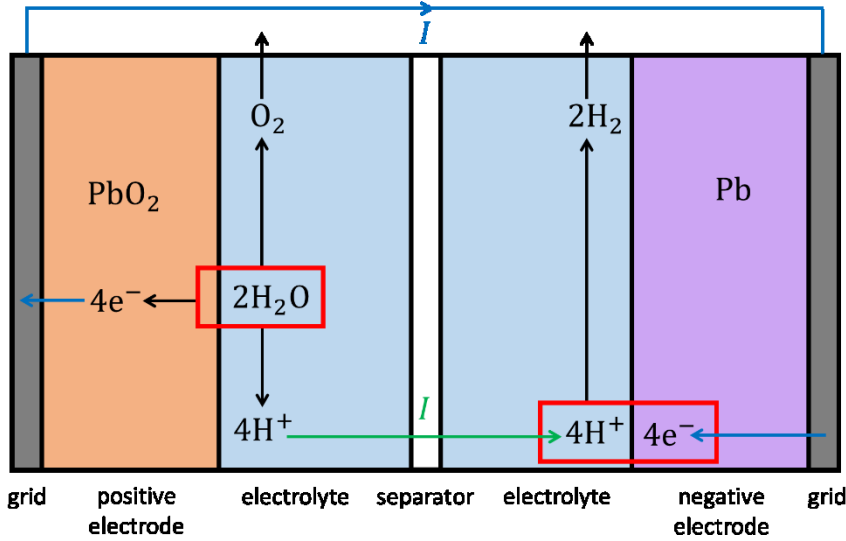
Figure 6   Electrolysis side reactions during charge of a LAB

The overall reversible reaction mechanism at the positive electrode is described as:

$$(\textbf{discharged}) \quad 2H_2O \leftrightarrow O_2 + 4H^+ + 4e^- \quad (\textbf{charged}) \tag{12}$$

and at the negative electrode as:

$$(\textbf{discharged}) \quad 4H^+ + 4e^- \leftrightarrow 2H_2 \quad (\textbf{charged}) \tag{13}$$
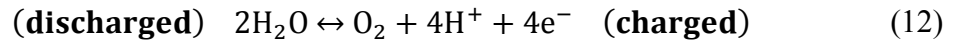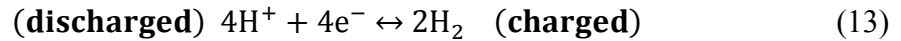
The equilibrium potential of the reaction at the positive electrode is 1.23 V relative to the standard hydrogen electrode, and that of the negative is 0 V since it *is* the standard hydrogen electrode [1]. This means that even at equilibrium conditions, the positive electrode of a LAB has an overpotential for producing O_2 gas and the negative electrode has an overpotential for producing H_2 gas. However, just as the main reactions of the positive and negative electrodes adhere to the Butler-Volmer relationship, so do the side reactions. Relatively large overpotentials are required for electrolysis to proceed at a significant rate in a LAB, and this typically occurs above 2.50 V for the whole cell [1]. For this reason, LABs are usually charged at or below this voltage. Conversely, the electrodes of a LAB should never fall below the equilibrium potentials of electrolysis reactions, so Eq. (12) and Eq. (13) should only ever proceed in the charging direction in a LAB.

When O_2 and H_2 gases are evolved at a significant rate, the amount of water in the electrolyte decreases, leading to a decline in total electrolyte volume and an increase in

electrolyte concentration. This means that long term operation of LABs requires periodic water replenishment, at least in the case of flooded/vented cells. In contrast to flooded LABs, sealed valve-regulated lead-acid (VRLA) batteries are maintenance-free. These special designs direct the evolved O_2 gas to the negative electrode, where the potential is well below 1.23 V. In this case, Eq. (12) will actually proceed in the discharging direction, but at the negative electrode. This recombines the O_2 and H_2 gases so that no significant amount of water is lost.

2.6.   Formation

When a LAB is first manufactured, the electrodes are electrochemically inactive plates. In order to make the battery useful as an energy storage device the manufacturer must subject it to its first charge, which is known as formation. The formation reactions have some similarities to the charging reactions covered in section 2.1, but in the case of formation the materials being converted at the electrodes do not start as $PbSO_4$. The following subsections will detail the processes involved in formation of LABs.

2.6.1.   Unformed Paste

Electrodes for LABs are made by applying a wet paste onto lead grids. The lead grids serve as a current collector which carries electrons to/from the electrodes. Both positive and negative plates have essentially the same initial paste composition, although expander-type additives are typically introduced to the negative plate paste [11] such that after formation its surface area will be more comparable to that of the positive plate. The wet pasted plates are then treated with a curing process which involves drying the plates in warm air. This evaporates any water and restructures the paste particles into a strong skeleton of PbO and basic lead sulfates connected to the grid through an intermediate corrosion layer [12]. A summary of the compounds making up the cured paste as given by Pavlov [11] is given in Table 2.

Table 2   Paste components

Name	Chemical formula	Description
Lead oxide	PbO	Component of original paste
Unoxidized lead	Pb	Component of original paste
Red lead	Pb_3O_4	Component of original paste
Water	H_2O	Mixed with original paste
Sulfuric acid	H_2SO_4	Mixed with original paste
Tribasic lead sulfate (3BS)	$3PbO\text{-}PbSO_4\text{-}H_2O$	Product of curing below 80 °C
Tetrabasic lead sulfate (4BS)	$4PbO\text{-}PbSO_4$	Product of curing above 80 °C
Monobasic lead sulfate (1BS)	$PbO\text{-}PbSO_4$	Product of soaking
Lead sulfate	$PbSO_4$	Product of soaking and early formation
Lead dioxide	PbO_2	Final formation product on positive plate
Sponge lead	Pb	Final formation product on negative plate

Different manufacturers will have their own specific recipes pertaining to the exact composition of their paste and the curing temperatures they use. Aside from the compounds in Table 2, various additives in relatively small quantities are sometimes used for improved performance. Carbon additives on the negative plate are one area of growing interest for improving performance in partial-state-of-charge cycling applications [13], [14]. The carbon has been found to form a capacitive system in parallel with the electrochemical system at the negative plate. This serves to attenuate the growth of insoluble $PbSO_4$ crystals in the electrode, thereby reducing progressive irreversible capacity loss and improving cycle life.

The cured plates can continue down one of two paths in the manufacturing process:

1) Tank formation: individual cured plates are assembled into large tanks of H_2SO_4 electrolyte and charged. The charged plates are then cleaned, dried, and stored as individual plates which can be assembled into containers at a later date before being sold and shipped. Electrolyte is then added to the cells by a local distributer.

2) Container formation: individual cured plates are assembled into containers to make unformed cells which are then filled with H_2SO_4 electrolyte. The assembled and filled cells are then subjected to the formation charge and are ready to be sold.

The formation process itself involves a soaking period (no more than a few hours) in which the cured plates sit in the electrolyte at open circuit, followed by the actual electrical charging process (up to several days) which electrochemically activates the paste material into charged positive and negative plates. During the soak, the H_2SO_4 reacts with the PbO and basic lead sulfates of the cured paste, producing $PbSO_4$. This reaction is exothermic, so the temperature rises significantly before the formation current is even initiated [15]. Once the formation itself begins, the plates that give up electrons will oxidize to form positive electrodes, while the plates that gain electrons will reduce to form negative electrodes. Subsections 2.6.2 and 2.6.3 will go into further detail on the reactions that occur at each electrode during formation.

2.6.2.   Positive Active Mass

The formation mechanisms of the positive active mass (PAM) are described by Pavlov [16] as a two-stage process. In the first stage, the PbO and basic lead sulfates are dissolved in the electrolyte forming Pb^{2+} and SO_4^{2-} ions. Depending on the availability of SO_4^{2-} ions, the Pb^{2+} ions will either crystallize into $PbSO_4$ or oxidize into Pb^{4+} to form PbO_2. These reactions have a low potential and replace dissolved SO_4^{2-} ions with water, reducing the concentration of the electrolyte to a slightly alkaline state. The first stage of formation is therefore characterized by a low voltage and high electrolyte pH.

Once the initial paste components diminish through conversion to $PbSO_4$ and PbO_2, the voltage rises and the second stage begins. At these higher voltages, $PbSO_4$ will dissolve such that Pb^{2+} ions can oxidize and form more PbO_2. The SO_4^{2-} released into the electrolyte increase the acid concentration and the pH decreases. Since the pH of the electrolyte affects the way the PbO_2 crystallizes, two distinct PbO_2 phases are created during formation. The high pH of the first stage produces orthorhombic lead dioxide (α-PbO_2) while the low pH of the second stage produces tetragonal lead dioxide (β-PbO_2). The distinction is an important one, as α-PbO_2 makes up the conductive skeleton structure of the PAM while the β-PbO_2 makes up the energetic structure that is converted to $PbSO_4$ during discharge. The condition of the skeleton contributes to the cycle life of the cell, while the energetic structure determines how much capacity can be discharged from the

cell. Both structures are crucial to the overall performance of the PAM and the battery as a whole, so the ratio of the two is an important consideration for a LAB manufacturer.

2.6.3.   Negative Active Mass

Similar to the PAM, the formation of the negative active mass (NAM) occurs in two stages [17]. The characteristics of low voltage and high pH during the first stage, and high voltage and low pH during the second stage apply to the NAM as well, but the species obtained from the NAM reduction are different from those obtained from PAM oxidation. During the first stage, PbO and basic lead sulfates will dissolve into Pb^{2+} and SO_4^{2-} ions. Depending on the availability of SO_4^{2-} ions, the Pb^{2+} ions will either crystallize into $PbSO_4$ or reduce into Pb and precipitate onto the electrode. The Pb structure formed during this first stage makes up the conductive skeleton of the NAM similarly to the α-PbO_2 of the PAM. As the formation transitions to the second stage, $PbSO_4$ will dissolve such that the Pb^{2+} ions will reduce and precipitate onto the NAM while the SO_4^{2-} ions serve to increase the electrolyte concentration. As electrons are transferred from the PAM to the NAM via the external circuit, H^+ ions migrate from the PAM through the separator to the NAM, thereby completing the circuit and balancing the excess charge of the SO_4^{2-} being released into the electrolyte. The Pb structure formed during the second stage makes up the energetic component of the NAM similarly to the β-PbO_2 of the PAM. The expander that is added to the paste of the NAM (mentioned previously in subsection 2.6.1) causes the energetic Pb to form smaller crystals, thereby increasing the surface area – and therefore the capacity – of the NAM.

2.6.4.   Theoretical Capacity

The theoretical capacity (TC) of a LAB is the amount of charge that would be required to form the battery if every electron transferred resulted in the conversion of PbO to PbO_2 in the PAM and Pb in the NAM. Since two electrons are transferred for every PbO molecule, and the atomic mass of PbO is known, the Faraday constant enables the calculation of the TC:

$$\frac{96485 \text{ A} \cdot \text{sec}}{1 \text{ mol e}^-} \times \frac{1 \text{ hr}}{3600 \text{ sec}} \times \frac{2 \text{ mol e}^-}{0.2232 \text{ kg of PbO}} = 240 \frac{\text{Ah}}{\text{kg of PbO}} \quad (14)$$

In practice, this can be applied by measuring the mass of the grids before pasting, and after pasting and curing:

$$TC = (Total\ Electrode\ Mass - Grid\ Mass - Water\ Mass) * 240 \qquad (15)$$

Because much of the applied charge will convert PbO to $PbSO_4$ in the first stage of formation, and also electrolyze water throughout the formation, the formation efficiency is less than 100% and the actual capacity required to completely form the battery will be greater than the TC. The required formation capacity will depend on the plate thickness, the paste composition, and the formation current, and can be more than double the TC [15], [18].

2.6.5.   Formation Charging Techniques

Since manufacturers want to optimize their production rate, faster formations are generally most desirable. At higher currents however, Joule heating can cause the cell temperature to rise above 60 °C, which will favor side reactions such as electrolysis and grid corrosion [15]. Thus, in order to use higher forming rates measures must be taken to remove heat from the cell. In tank formation, the relatively large volume of electrolyte is enough to dissipate heat, but when the electrodes are charged in a series of tightly packed containers, heat dissipation becomes a problem [15]. This is addressed in industry by immersing the cells in a cooled water bath [19], or by circulating the electrolyte of the cells through a cooling system [15], [20].

While constant-current formation algorithms are the simplest to employ, they are less accommodating to the formation mechanisms than are more complex algorithms such as those described by Weighall [19]. For example, due to the high soaking temperature and low electrical conductivity of the cell at the beginning of formation, it is common for low starting currents to be used. Once the temperatures relax into the preferred range for formation (30 °C to 50 °C according to Pavlov [15]), the current can be safely increased. Towards the end of formation however, most of the applied current will be driving side reactions (particularly the electrolysis of water as discussed in section 2.5) which makes the formation inefficient. Reducing the current at the end of formation helps to alleviate this inefficiency.

Another common technique described by Weighall involves partially discharging the battery before completing the formation, which is done to counteract a particular phenomenon that occurs during LAB formation. Pavlov [16] has shown that in some cases converted active material will form a shell around unconverted inactive material, essentially blocking it from being converted even after extensive formation. Discharging the cell removes the shell of active material and expedites more complete conversion when the formation is resumed. Without the discharge during formation at the factory, this material could only be converted through cycling by the end-user. Many different pulse-charging strategies have also been studied. Kim and Hong [21] have shown that pulsing to brief rests or brief discharges during the formation help alleviate concentration gradients, while Kirchev *et al*. [8] found that the pulses reduce the average overpotential, reducing gassing and therefore improving charge efficiency.

2.6.6. Termination

LAB formation can be terminated over a broad range of formation times. If a small amount of inactive material is left unformed, proper charging by the end-user will activate the extra capacity. As mentioned in the previous subsection, some material can only be converted through operational cycling anyway, unless special formation techniques are used. Regardless, manufacturers of LABs must find a balance between forming cells to a minimal level to increase production rates, and forming cells excessively to maximize product performance. When product performance is favored, the formation can still be conducted efficiently if the manufacturer can detect when the diminishing returns reach a strategic threshold. Pavlov [15] lists the following criteria for identifying when a formation is complete:

1) Unchanging electrolyte concentration
2) Unchanging rate of gas evolution
3) Metallic tracks can be achieved by scratching of the formed NAM
4) Dark coloration of the formed PAM
5) Chemical analysis to determine the composition of PbO_2 in the PAM and Pb in the NAM

Criterion 1) can be checked with a handheld meter periodically as a formation proceeds. Unfortunately, even if no more SO_4^{2-} ions are being released into the bulk electrolyte through conversion of inactive $PbSO_4$, the loss of water through electrolysis means that the electrolyte concentration will continue to increase even after formation has completed.

Criterion 2) requires an auxiliary system for collection and analysis of evolved gases for direct measurement, but likely could be put to practice. Henn *et al.* [22] used Raman spectroscopy to measure gas evolution rates in sealed VRLA batteries, but this must be done invasively and would not be a practical solution in mass production. For vented cells, the naturally released gasses from any number of cells undergoing formation in a controlled enclosure could be measured in situ, but the capital costs associated with such a complex system may not appeal to a manufacturer.

Criteria 3) and 4) can be put to practice relatively easily for tank formation, since the electrodes are fully accessible for visual inspection throughout the formation. For container formation however, this method would require disassembly of cells and is therefore impractical.

Criterion 5) requires advanced equipment and time for sample analysis which are obvious obstacles for battery manufacturers. D'Alkaine *et al.* [23] developed a relatively simple chemical analysis method that involved dissolving the entire positive electrode material in a solution, allowing for the percentage of PbO_2 in the formed electrode to be measured. This method could be used for evaluating formations after they have already completed as an iterative approach to determining benchmark formation requirements for each battery model produced by the manufacturer. However this would not be nearly as advantageous as a technology that would enable any given formation to be properly terminated regardless of the electrode properties and environmental conditions.

Aside from these five criteria, the default method used by some manufacturers for terminating formation is nothing more than a predetermined capacity or time limit based on generalized empirical algorithms. This method is certainly simple and inexpensive to employ, but leaves much to be desired as it takes in no information specific to the ongoing formation that would indicate its completeness. Podrazhansky and Tsenter [24] and

Mckinley *et al.* [25] proposed charging techniques that involve using the changing internal resistance of the battery during formation to indicate when charging is complete. Research methods involving battery internal resistance (or more generally, impedance) will be discussed in the next section.

2.7. Battery Impedance Measurement

An abundance of scientific studies have explored methods and applications for measuring the resistive, capacitive, and even inductive characteristics of batteries. The lumped real and imaginary components of these parameters together make up the overall impedance of the battery.

2.7.1. Equivalent Circuit Modelling

There are a wide range of equivalent circuit models used in literature to represent the working voltage of a battery, E. Perhaps the most well-known of these circuits is the Randles model [26], shown in Figure 7. This circuit models the EMF of the battery as an ideal voltage source, which provides the unloaded voltage of the battery in equilibrium. The ohmic resistance of the metallic components as well as the electrolyte and separator are modelled as the series resistor, R_o; the charge-transfer resistance for activation polarization across the EDL is modelled as the parallel resistor, R_{ct}; the parallel capacitor, C_{dl}, is used to model the capacitance of the EDL; the high-frequency inductance of the metallic components is modelled by the series inductor , L; the Warburg impedance, Z_W, is a constant phase element and is the simplest method for modelling mass transport effects [27]. This model serves reasonably well for qualitatively describing equilibrium and non-equilibrium conditions of a battery. When the circuit is open, the battery voltage is equal to the EMF. When an external current begins to flow, there is an immediate ohmic loss through R_o while overpotential of the EDL takes time to establish due to C_{dl}. At the same time, Z_W increases the EDL activation overpotential from R_{ct} when mass transport effects come into play. When the external current stops, C_{dl} must self-discharge through R_{ct} and Z_W before equilibrium can be achieved. The model also shows how the EDL capacitance, the Butler-Volmer relationship, and mass transport effects will all contribute to the time constant inherent to the charging and discharging of the EDL.
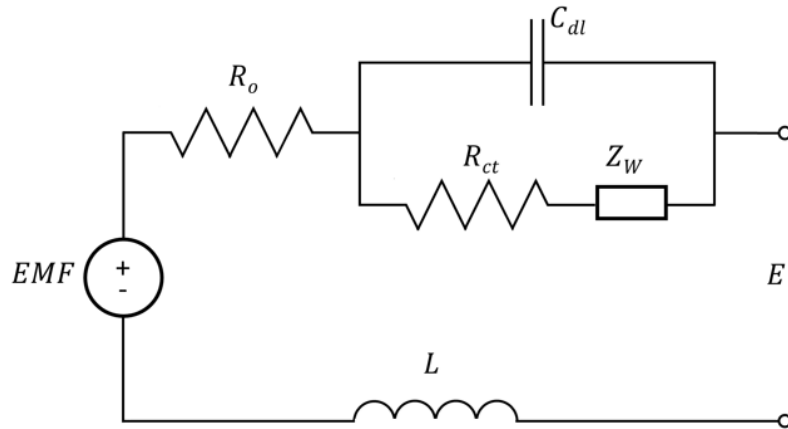
Figure 7   **Randles model representing a battery**

For precise modelling of battery behaviour however, the Randles model has significant shortcomings. The theory presented previously in this chapter makes it clear that the parameters of the Randles model will not remain constant during operation. V_{EMF} and R_o are dependent on SOC, and R_{ct} is dependent on a number of variables based on the Butler-Volmer equation. Additionally, while the parameters in Eq. (11) will remain constant for a conventional capacitor, they are highly variable in the EDL of a battery or supercapacitor. The available reaction surface area, A, will depend on how much material has already been converted, and the activation overpotential will strongly influence the compactness of the EDL, d [7]. Furthermore, the negative and positive electrodes will have their own individual variations for each parameter, which make the lumped parameters of the Randles model even less representative of a physical cell.

A great variety of more complex models have been presented in literature to account for the shortcomings of the basic Randles model. In their study of VRLA batteries, Ng et *al.* [28]   used an empirical method to account for the high variability of R_{ct} and C_{dl}. By measuring the battery voltage in the first few minutes after open-circuiting, their formula was able to accurately predict the EMF that would only be realized after hours of relaxation. As discussed in section 2.2, knowledge of the EMF of an operational LAB can be used to estimate its SOC, so reducing the open circuit time necessary for this measurement is of clear benefit for end-users. Ghandi [29] improved upon existing models by accounting for decreasing active surface area of LAB electrodes during discharge. This was done through the use of variable ohmic resistance and a dynamic multiplier intended to modify the area

term, *A*, in the Butler-Volmer equation. The improved model compared well with experimental discharging voltage profiles, which can typically only be accomplished through curve-fitting parameters lacking physical meaning [29].

In order to account for side reactions during charging at high SOC, additional modifications must be made to the Randles model, such as that shown in Figure 8. This model illustrates how the current at both electrodes (+ and −) will be shared between the gassing reactions and the main charge-transfer reactions, depending on their relative reaction resistances. The model presented by Thele *et al.* [30] employs a similar method for modelling both vented LABs and VRLAs. The authors also modelled Pb^{2+} availability at each electrode and used non-linear elements to account for the high variability of the internal conditions of the battery. Validation against experimental data gave good results, hinting towards potential applications in hybrid vehicles and regenerative braking technology.
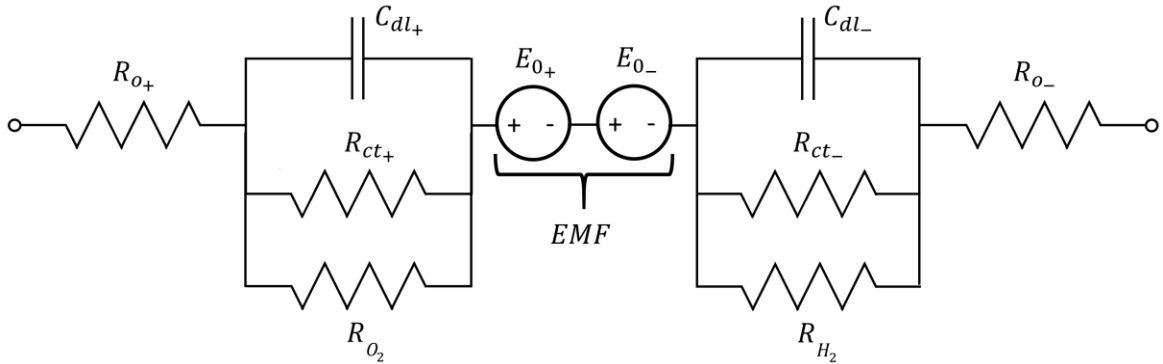
Figure 8   **LAB equivalent circuit accounting for electrolysis side reactions**

2.7.2.   AC Injection Methods

One widely used experimental technique in the research of internal battery characteristics is electrochemical impedance spectroscopy. This method involves injecting low-amplitude alternating current (AC) into the battery at a wide range of frequencies (typically millihertz to megahertz) and measuring the corresponding AC voltage response and phase angle. The battery impedance as a function of frequency can then be calculated:

$$Z = \frac{E}{I}$$

(16)

$$Z_{\text{Re}} = Z \cos \theta \tag{17}$$

$$Z_{\text{Im}} = Z \sin \theta \tag{18}$$

where

Z is the complex impedance, in Ω

I is the injected alternating current, in A

E is the measured alternating voltage response, in V

Z_{Re} is the real component of the complex impedance, in Ω

Z_{Im} is the imaginary component of the complex impedance, in Ω

θ is the measured phase angle between I and E

By performing these measurements and calculations over a wide range of frequencies, Nyquist plots of Z_{Im} vs. Z_{Re} can be created and interpreted in order to identify values for each parameter in the equivalent circuit model. Huet et *al.* [31] used this technique to measure the resistance for a LAB at a specific frequency and evaluate its potential as an indicator of online SOC. By using a frequency that minimized the imaginary component of the complex impedance, the measured impedance could be interpreted as the ohmic resistance. A reference electrode was also used such that the voltage response from both the positive electrode and negative electrode could be isolated. It was concluded that while the measured resistance was clearly dependent on SOC, its dependence on other factors such as current magnitude made it impractical as a universal parameter for identifying SOC during operation.

Buller et *al.* [32] used electrochemical impedance spectroscopy to assign variable values to the equivalent circuit elements, and produced results for R_{ct} that strongly resembled the Butler-Volmer relationship. The collected data was then used to simulate operational behaviour of a LAB, which compared well against experimental data.

2.7.3.   DC Pulsing Methods

Direct current (DC) pulsing involves a sudden, temporary change in the charging current or discharging current of a battery. Through Ohm's law, the effective resistance of the battery can be calculated from the voltage change that results from the current change.

An important consideration is that the duration of the pulse will influence the measured resistance. The ohmic response will occur instantaneously, after which the EDL will charge or discharge to a new equilibrium voltage. The new equilibrium voltage will be a function of the changing reaction resistance that results from the pulse, according to Butler-Volmer. Thus, the longer the pulse, the greater the measured voltage change will be. Due to the non-linearity of Butler-Volmer, the measured resistance will also depend on the magnitudes of both the pre-pulse current and the pulse current.

As mentioned in subsection 2.6.4, many pulsing techniques have been employed as a method to improve charging and formation efficiency for LABs, but few of these studies attempt to use the pulses as a method of calculating the internal resistance of the battery. Hande [33] used DC pulse resistance measurements for estimating internal battery temperatures, but the bulk of literature pertaining to evaluation of SOC through DC pulse resistance were found in patents. McKinley *et al.* [25] developed a technique for applying DC pulses during the formation charge of LABs. Their patent application claims that by capturing the immediate voltage response (less than a millisecond) to a current pulse, the ohmic resistance of the battery can be measured. They also claim that the changes in these resistance measurements can be used to indicate when the formation should be terminated, but no theoretical background for this claim is provided and no supporting experimental data is reported. Longer pulse durations do not appear to be studied in any significant capacity for LABs.

Chapter 3   Methodology

Based on the reviewed literature and identified objectives, a series of experiments were designed and conducted in order to investigate the potential for internal resistance measurements to indicate the completeness of a LAB formation. While the majority of these experiments were run in the laboratory, tests were also carried out in an actual LAB manufacturing plant. This chapter will describe in detail the methods used throughout experimentation.

3.1.   Test Cells and Equipment

Surrette Battery Company Limited (SBCL) provided unfilled, unformed LABs for testing, as well as H_2SO_4 electrolyte for filling the cells prior to formation. All tests were conducted on vented cells due to their availability and simplicity, including the different sets listed in Table 3 with the calculated TCs of each electrode. The TCs are calculated from sensitive data provided in confidence by the manufacturer. For all cells the PAM has a larger TC, indicating more paste mass on this electrode.

Table 3   **LAB test cells**

Cell set	Model name	Quantity tested	Configuration	PAM TC (Ah)	NAM TC (Ah)
A	S-480	3	6 V	710	535
B	S-480	7	2 V	710	535
C	16 CS 15 P	7	2V	1165	1043

Note that set A and set B are the same model with the exception that the A cells were preassembled into a 6 V module consisting of three cells in series. Both set B and set C came from the manufacturer as individual 2 V cells. The reason for testing two different models is to verify that any findings regarding internal resistance apply to more than one cell type. Full specifications for both models can be found in Appendix A.

Table 4 lists the test instruments used during experimentation. A power-cycler was used to form, discharge, and charge the cells while logging measurements of current, voltage, cell temperature, and ambient temperature. The power-cycler logs the voltages of positive and negative half-cells through use of a mercury/mercurous sulfate (Hg/Hg_2SO_4) reference electrode placed into electrolyte at the top of select cells. The programmable cycling

schedules of the power-cycler enabled a variety of precise DC pulsing strategies to be employed for internal resistance measurements during formations. Aside from these pulsing strategies, a hand-held battery analyzer was also used to collect internal resistance data through AC injection. Throughout formation and subsequent cycling, the SG and temperature of the bulk electrolyte at the top of the cells were measured using a digital portable density meter, where the SG readings were automatically corrected to 20 °C by the meter. Finally, digital multimeters were used to verify the measurements being recorded by the power-cycler. An uncertainty analysis of key measurements and calculations can be found in Appendix B.

Table 4   Test instruments used

Measurement	Instrument
Power-cycling, current, voltage, and cell temperature	Arbin BT2000 #175099 with 3 channels each rated 0-20 V and ± 100 A (Used with Omega T-type thermocouples for temperature) (Used with Hg/Hg$_2$SO$_4$ reference electrode for half-cell voltages)
Electrolyte SG and temperature	Anton-Parr DMA 35 portable density meter
AC impedance	Fluke BT510 battery analyzer
Voltage verification	Fluke 87 multimeter
Current verification	Fluke 336 clamp meter

3.2.   Setup and Safety

Figure 9 shows the typical setup for a test cell undergoing formation in the laboratory. The room is well ventilated by exhaust fans to prevent a build-up of flammable gases generated during formation. Some trace amounts of hydrogen sulfide fumes can also be released during formation, and the condensing tower attached to the fill port of the cell acts to mitigate this. The fill port of the battery is used for electrolyte addition as well as for taking SG measurements. Current cables and voltage probes were connected to the terminals of the batteries using brass nuts and bolts for low electrical resistance. External wall temperature probes consist of T-type thermocouples secured to the cell casing with insulating tape, while the internal temperature probe is a Teflon-coated T-type thermocouple that is placed through a small hole drilled into the cell casing. This probe is gently inserted between two plates near the middle of the cell and is long enough to reach the centre of the electrodes, thus measuring the highest temperatures in the cell during

operation. Since only one internal temperature probe and one reference electrode were available, these two measurements could only be applied on select cells.

All test cells were placed in spill containers during formation and subsequent cycling, and all spill containers were placed on mobile carts. The current disconnection point allows for test cells to be disconnected and transported as necessary. Limits and alarms were set in the software to shut down the tests when abnormal currents, voltages, or temperatures are reached. The power-cycler and test cells can also be monitored remotely using webcams and through remote-access to the computer which runs the software. Proper PPE was worn at all times, including safety glasses, lab coats, gloves, steel-toed footwear, and face shields.

It should be noted that in order to measure the voltages of the individual cells in set A, custom voltage-taps had to be installed by drilling through the top of the module casing and into the bus-bars that connect the three cells within. This is depicted in Figure 10. While the external wall temperature probe are not shown, three thermocouples are attached to the cell such that each senses the temperature of one of the three individual cells.
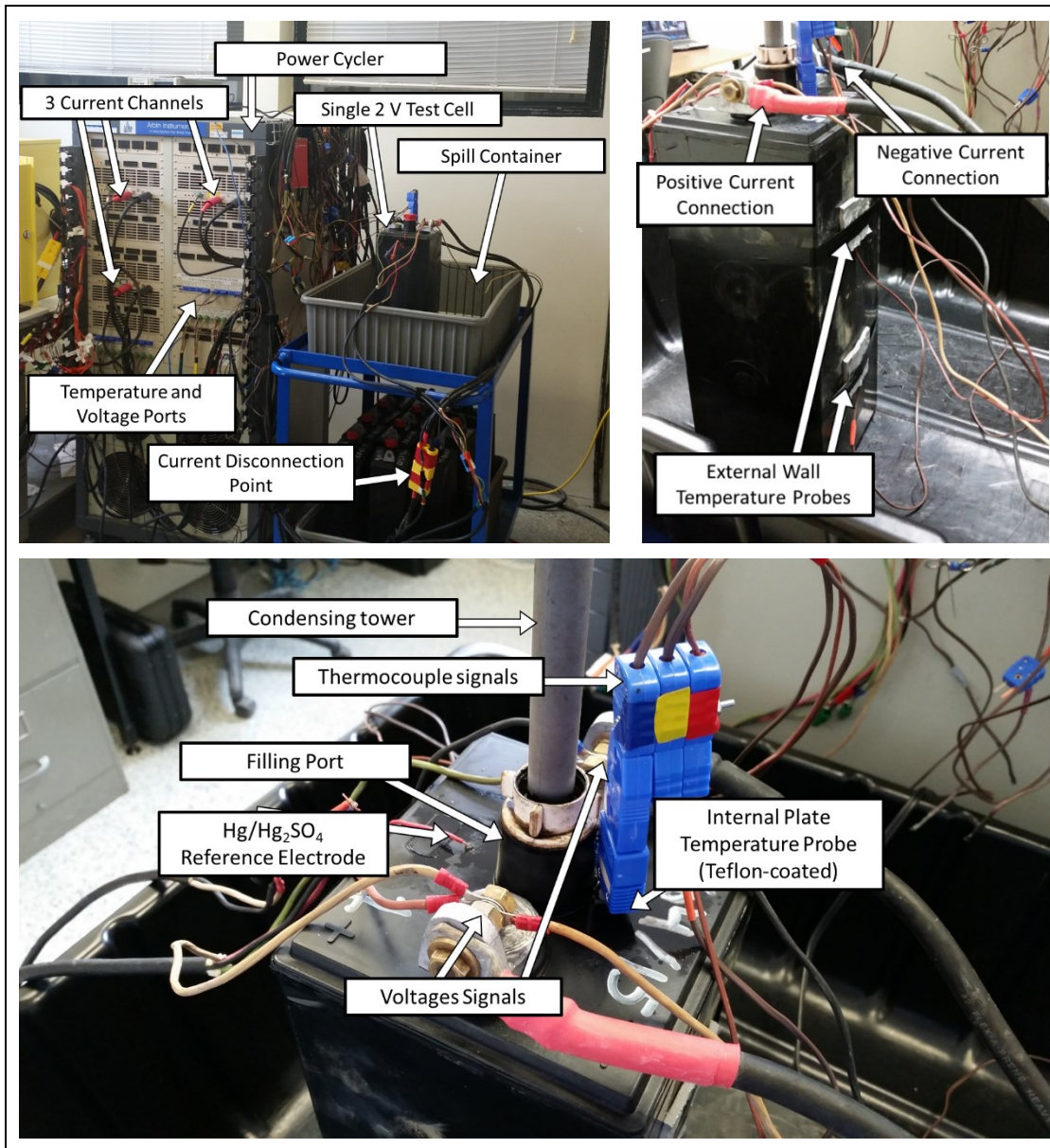
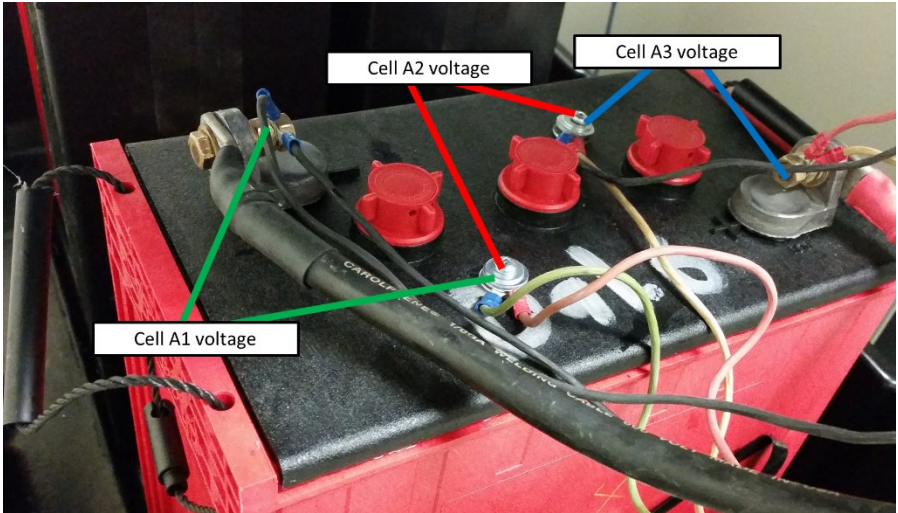**Figure 9** **Experimental apparatus for test cells (cell C6 shown)**

Figure 10   Voltage measurement for cell set A

3.3.   Formation Techniques

Only container-formations of pre-assembled cells were performed in this study, due to the complexities and safety concerns associated with the alternative tank formation method. Once all measurement systems were connected and data logging had begun, test cells were filled with 1.200 SG electrolyte to begin the soaking process. The formation current was turned on after a soaking period of 80 minutes, although when multiple cells were filled sequentially on the same channel the soaking period would inherently vary by a few minutes for each cell. Simple strategies were employed with regard to the base current (as opposed to the pulse current) used during formations, although lower initial base currents were used at the start of formation to mitigate high soaking temperatures in excess of 50 °C. Table 5 lists the current steps used for each cell set. For the A cells the current was initially started at 20 A, but, noting that the cell temperatures were continuing to rise in the first hour, this current was reduced to 10 A. After 6 hours at 10 A, the current was returned to 20 A for the remainder of the formation. For set B the recommended container-formation charging algorithm from SBCL was employed. This entails forming at 20 A for the first day, 30 A for the second day, and 40 A thereafter. This procedure was followed except for an initial 2-hour period at 10 A, again to mitigate the high soaking temperatures. After observing how changes in the base current cause sudden changes in the internal resistance trends during formation, it was decided that subsequent formations should avoid current

33

steps after the initial high temperature period. Thus for the set C formation the current was stepped up to the final base current relatively quickly.

Despite the fact that the TC of the C cells is 64% higher than that of the B cells, the specifications for the two cell models (Appendix A) show that the dischargeable capacity is only about 40% higher at slower rates and about 20% higher at faster rates. This is likely due to the fact that the additional material in the C cells comes from plate thickness, not plate area (see specifications in Appendix A). For thicker plates it is difficult to access the material in the deeper pores, and this effect is more pronounced at faster rates. Since formations are conducted at faster rates, the final current for the C cells was chosen to be 20% higher than that for the B cells, which gives 50 A.

Table 5   **Steps in base current used during formations**

Cell set	Step 1	Step 2	Step 3	Step 4
A	20 A for 1 hour	10 A for 6 hours	20 A for 235 hours	N/A
B	10 A for 2 hours	20 A for 21 hours	30 A for 24 hours	40 A for ≤ 72 hours
C	20 A for 3 hours	30 A for 2 hours	40 A for 2 hours	50 A for ≤ 94 hours

In some tests single cells were set up on their own channel, while in other cases several cells were connected in series on the same channel in order to make better use of equipment. In the latter case, individual cells were sequentially removed from the string after a predetermined formation capacity had been applied. In this way, the internal resistance and discharge capacity of formed cells could be compared for a range of formation inputs. Since the individual A cells were constrained inside the same module, removal of individual cells during formation was not feasible. For set B and set C however, this was the strategy employed. The power-cycler has a maximum voltage rating of 20 V per channel, and since cell voltages can exceed 2.8 V during formation, no more than six cells could be safely connected in series for a given test. Table 6 summarizes how the cells were arranged and formed for set B and set C. With seven cells in each set, at least one cell had to be formed individually. For set C however, two cells were intentionally formed individually for reasons that will be addressed in the next section.

Based on previous tests conducted by the researchers, it was expected that the B cells would be nearing a fully formed state between 1800 Ah and 2500 Ah, so the selected formation

levels were centered on this range. No previous formations had been conducted on the C cells however, so the range of formation levels were chosen as round multiples of the 1165 Ah PAM TC, which is the highest of the TCs for the two electrodes of this cell type. Since the PAM should continue forming after the NAM has fully formed, the PAM TC better represents the TC of the full cell and is therefore selected as the reference value.

Table 6   Summary of group formations

Cell ID	Setup	Formation Capacity Applied (Ah)	% of Theoretical Capacity Applied
B1	Individual	1000	141
B2	String B	1333	188
B3	String B	1667	235
B4	String B	2000	282
B5	String B	2500	352
B6	String B	3000	423
B7	String B	4000	563
C1	String C	1166	100
C2	String C	1751	150
C3	String C	2334	200
C4	String C	2913	250
C5	String C	3733	320
C6	Individual	4315	370
C7	Individual	4894	420

Throughout formation, the power-cycler software logged current, voltage, cell temperature, and ambient temperature every 6 seconds. This logging speed was increased during the pulses, as will be discussed in the next section. Cells formed to higher levels underwent extensive electrolysis, leading to substantial depletion of the electrolyte volume inside the cells. To prevent the electrolyte level from falling below the top of the plates, replacement water was added to the cells as necessary. After each cell was formed it was topped up with 1.265 SG electrolyte as recommended by SBCL.

3.4. Internal Resistance Measurements: AC Injection

AC injection was accomplished with a Fluke BT510 battery analyzer. Like many handheld battery resistance meters, the BT510 injects AC current into the battery at a single frequency as opposed to electrochemical impedance spectroscopy which injects a wide range of frequencies. The single frequency is intended to be high enough that the EDL will

not respond enough to contribute to the measured voltage response, but not so high as to pick up on inductive effects in the metallic components (analogous to shorting the parallel capacitor in the equivalent circuit). In this way, only the ohmic resistance of the metals, electrolyte, and separator should be measured. The possibility of employing electrochemical impedance spectroscopy in this study was explored but ultimately ruled out, as it is impractical for use in an industrial battery manufacturing setting.

The BT510 battery analyzer has a positive and a negative probe which the user must press against the positive and negative terminals of the battery, respectively. The device then injects a 100 mA signal into the battery at 1 kHz and displays the calculated resistance on a screen. The user can then save the measured resistance and the cell voltage once the readings have stabilized to satisfaction. At each measurement interval multiple measurements were taken until it was felt that an accurate average had been obtained. This typically required between 3 and 6 measurements per interval. It was expected from theory that the highest ohmic resistance should be present in the early stages of formation, declining quickly as the bulk of the inactive material is converted. For this reason, manual AC injection measurement intervals were expanded as formation progressed past the early stages.

3.5. Internal Resistance Measurements: DC Pulsing

To measure more than just the ohmic resistance, the base formation current was pulsed briefly throughout the formation. Pulses were scheduled to occur every 50 Ah of formation and were held for 10 seconds. During each DC current pulse, the voltage response was measured as frequently as the power-cycler was capable (every 16 milliseconds) in order to capture the fast ohmic voltage response on the first data point, thereby enabling isolation of the ohmic resistance from the reaction resistance.

Table 7 lists the pulsing strategies used on each cell set. Since it is possible to pulse up or down from the base current, both methods were employed during the first experiment, which was conducted on the A cells. After examining the results (see section 4.4), only upward pulses were employed for the formations of set B and set C. Since the B cells held different base currents for significant portions of the formation, the pulse could either be

set to a fixed current difference (e.g. always + 30 A) or a fixed current value (e.g. always to 60 A). Either choice would cause the resistance to shift when the base current changes (due to Butler-Volmer behaviour), so the latter option was arbitrarily chosen. For the C cells, the relatively fast step-up to the final base current made both options essentially the same.

Table 7   Pulsing strategies applied during formation

Cell Set	Base Current (A)	Pulse Up (A)	Pulse Down
A	10, 20	Base + 20	Base − 10
B	10, 20, 30, 40	Base to 60	N/A
C	20, 30, 40, 50	Base + 30	N/A

After examining the results of the set B formation, a modification was made to the pulsing strategy for the set C formation. In order to improve the smoothness of the observed resistance trends, three back-to-back pulses were used for every interval in the formation, allowing for averaging of the individual pulses. The period between pulses was set to be as long as the pulse duration to allow the voltage transients to dissipate before the next pulse.

The power-cycler also has a built-in function for measuring battery resistance. The function takes in a pulse amplitude in amps and pulse duration in milliseconds, and outputs a value in ohms. According to the product manual [34], the function imposes 10 of the specified current pulses back-to-back and averages the calculated values, where one "pulse" consists of a pulse-up, return, pulse-down, return. Although logging only occurs every 16 milliseconds, this built-in function uses pulse durations as short as 1 millisecond. This function was only explored after the formations of set A and set B had completed.

The function can only be applied on the channel as a whole, so when several cells are in a string it is the resistance of the entire string that is measured. Since cells are sequentially removed from the string during the formation, the resistances of the interconnections have to be accounted for, and this degrades the reliability of the measured resistance trend. To avoid this, cell C6 and cell C7 were formed as individual cells on their own channels. Since these cells were formed the longest, the resistance trends are of most value to these cells. Cell C7 was formed first, employing the function with a single 1 millisecond pulses. In

order to improve the observed trend, cell C6 was also formed using the function with 1 millisecond pulses, but three times back-to-back at every pulse interval for averaging.

3.6. Discharge Tests

In order to evaluate the available capacity in each cell provided by formation, the cells were subjected to discharge tests. After cells had been formed and topped up with 1.265 SG electrolyte, they were left to rest for at least 12 hours such that their temperatures could return to an ambient level. Using the same power-cycler and experimental setup used in formation, a constant current was then drawn from each cell until its voltage fell to a set limit, after which point the cell rested again. It is common practice to set the voltage limit to 1.75 V per cell on discharge, as the rate of voltage decline usually becomes exponential near this point. The discharged capacity at the time this limit was reached was recorded for each cell. Since cells formed to higher levels should take longer to reach the discharge voltage limit, cells could not be arranged in series on discharge as they had been during formation. Each cell was discharged individually on its own channel.

Discharge rates for batteries are typically given in terms of a C-rate, which is the current required to discharge the battery in one-hour. A C/4 rate is the current required to discharge the battery in 4 hours, which is an established laboratory standard for discharge testing. The cell specifications provided in Appendix A give the C/4 current to be 61 A for the A cells and B cells, and 74 A for the C cells. These were the discharge currents used.

3.7. Data Analysis

All recorded data was analyzed in spreadsheets. The combined interest of exploring very short pulse times (16 milliseconds) and relatively long pulse times (10 seconds) for dozens of pulses throughout a variety of lengthy formations resulted in many millions of data points being produced. Thus, formulas were developed for rapid filtering of the bulk data in order to retrieve the current and voltage immediately before each pulse and at a desired point within each pulse. The internal resistance was then calculated as follows:

$$IR_t = \frac{E_t - E_0}{I_t - I_0} \tag{19}$$

where

t is the time after the pulse, ≤ 10 s

IR_t is the internal resistance at time t, in Ω

E_0 is the cell voltage immediately before the pulse, in V

E_t is the cell voltage at time t, in V

I_0 is the base current, in A

I_t is the pulse current, in A

Once internal resistance values were obtained, a simple technique was employed to evaluate how the resistance was changing throughout the formation. This is referred to as the differential resistance:

$$DR_j = \frac{IR_j - IR_{j-x}}{Cap_j - Cap_{j-x}} \tag{20}$$

where

j is the integer referring to the present pulse interval, ≥ 2

IR is the internal resistance, in mΩ

Cap is the formation capacity, in Ah or as a percentage of PAM theoretical capacity (%TC)

DR is the differential resistance, in m$\Omega \cdot$ Ah^{-1} or m$\Omega \cdot$ (%TC)$^{-1}$

x is the number of pulsing intervals over which DR is to be calculated

The discharge capacity for a given cell and current will increase with temperature, as higher temperatures improve the conductivity and reaction kinetics of the cell. Therefore, in order to properly compare the capacities discharged from the cells in this study, a temperature correction had to be taken into the analysis. The International Electrotechnical Commission [35] provides a formula for this correction:

$$Cap_r = \frac{Cap}{1 + \lambda(T_1 - T_r)} \tag{21}$$

where

T_r is the desired reference temperature, taken as 25 °C for this study

Cap is the measured discharge capacity before correction

Cap_r is the discharge capacity corrected to reference temperature T_r

T_1 is the measured temperature at the start of the discharge

λ is a constant given as 0.006 K^{-1} for currents slower than C/3 (this study) and 0.01 K^{-1} otherwise

Thus all discharge capacities are corrected to 25 °C for proper comparison. In order to minimize errors introduced by the correction, cell temperatures were kept within 2 °C of the reference temperature before discharging.

3.8.   Experiments at Surrette Battery Company

SBCL granted permission for experiments to be carried out in their factory. This allowed for a verification test of the internal resistance method in an industrial setting. SBCL has four methods for forming batteries, all of which were briefly described in Chapter 2:

1. Container formation
2. Water-bath cooled container formation
3. Electrolyte-circulation cooled container formation
4. Tank formation

Of the four formation lines, the only one presently equipped to log voltage and current measurements is the water-bath, so this line was chosen for the experiment. The water-bath consists of a large chamber which holds the batteries, as shown in Figure 11. The chamber is filled with water which is circulated through an external cooling system during formation. The resulting heat-removal through the cell walls allows the batteries to be formed at much higher currents than would be allowable in the uncooled laboratory formations.

For this experiment, the modules that were formed were the same as the set A module formed in the laboratory (6-Volt S-480 model). Seventy-two of these 6 V modules can be loaded into a single water-bath, making up two strings of 36 modules (or 108 cells) each. The S-480 modules are shown connected in series during formation in Figure 11. The chamber is typically left with the wickets closed during formation such that any released gases can be exhausted by the ventilation system. The charger is made by Digatron, featuring 8 channels each rated for ± 80 A and 375 V.

Figure 11　　Experimental setup for water-bath formation at SBCL

For this experiment, one of the 36-module strings was assigned as the 'resistance string', while the other was assigned as the 'discharge string'. Individual modules were sequentially removed from the discharge string at predetermined stages of the formation and subsequently subjected to a discharge test in the factory. In contrast, the resistance string was left intact with all 36 modules for the entire formation. This was done with the expectation that the measured resistance trends would be much easier to analyze if the string did not have cells continually being removed.

The typical formation algorithm for the water-bath is not as simple as the ones used in the laboratory. After 3 hours at 22 A to start the formation, the current is temperature-dependent, switching between the main base current of 75 A and a cool-down current of 55 A as the measured battery temperatures vary. On one hand, this allows for resistance measurements to be taken every time the current changes, without making any

modifications to the algorithm. However, after inspecting records of past formations, it was found that this technique would not provide enough data points. Thus additional steps had to be inserted into the relatively complex existing charging schedule. The software logs data every minute in this existing schedule, but it is capable of logging every second.

The scheduling software was not as versatile as the one used with the power-cycler in the laboratory, making it difficult to implement the desired number of pulsing instances without modifying the existing formation strategy beyond the manufacturer's wishes. Furthermore, since the base current of 75 A was already near the maximum rating of 80 A, the pulse-up technique could not be used. In the end, the schedule was modified such that the current would undergo three back-to-back 15-second downward pulses between the base current of 75 A and a pulse current of 45 A, while logging every second. The required cooling periods made it such that pulse intervals would vary between 50 Ah and 100 Ah. Both the resistance string and the discharge string formed according to this schedule.

The discharge tests were carried out on a number of discharge-capable channels throughout the factory as they became available. As in the laboratory, batteries were given time to cool to near 25 °C before discharging. The channels used did not permit automatic termination of the discharge when 1.75 V per cell was reached, nor did they allow for logging of data. Therefore, manual current and voltage measurements had to be recorded for each module throughout the discharge, which was done at a C/4 rate as in the laboratory tests. As the voltages neared 1.8 V per cell, measurements were taken more frequently such that the discharge could be terminated as near to 1.75 V per cell as possible. Temperature and SG measurements were also manually taken at the start and end of discharge so that the discharge results for the test modules could be properly corrected and compared.

Clearly, the level of control over experimental conditions was drastically reduced for the factory testing, as might be expected. However, the level of precision was not required to be as high as in the laboratory testing, as the factory tests were more for proof-of-concept verification than exact quantification.

Chapter 4 Results and Discussion

This chapter presents the significant findings of this study, starting with the more general results pertaining to the cell voltages, temperatures, and electrolyte SGs obtained during formation. Then, the internal resistance results during formation will be discussed at length including rationalization based on the previously presented theory. Next, these results will be compared to the dischargeable capacity that was obtained by forming to different levels, showing that the internal resistance does indicate when negligible enhancement of dischargeable capacity is obtained from further formation. Finally, results from an experimental deployment of the pulsing method in a LAB manufacturing plant will be discussed.

4.1. Filling and Soaking

Figure 12 provides an example of the measurements taken during filling and soaking of cells prior to formation, including the electrolyte SG and temperature measured manually with the density meter as well as the cell wall temperatures measured every 6 seconds by the power-cycler. The data represents the first formation test, in which one 6 V module of set A was filled with electrolyte and allowed to soak for 80 minutes before the formation current was switched on. Since the 6 V module contains three 2 V cells, each cell had to be filled and monitored individually. The cells were filled sequentially, resulting in a delay of several minutes between the start of one cell filling process and the next. The individual filling periods are clearly represented by the 6-second temperature measurements, with each cell temperature starting to rise at different times as the exothermic soaking reactions begin. The temperatures rise throughout the soaking period to 45 °C, and continue to rise when the formation current is turned on. The manual measurements of electrolyte temperature reveal a temperature difference between the inside and outside of the cell that is as large as 10 °C during the soak. For all cells, the SGs fall sharply from the original 1.200 SG of the electrolyte supply, an expected observation given that the SO_4^{2-} ions in the electrolyte are converted to $PbSO_4$ in the paste material during the soaking period.
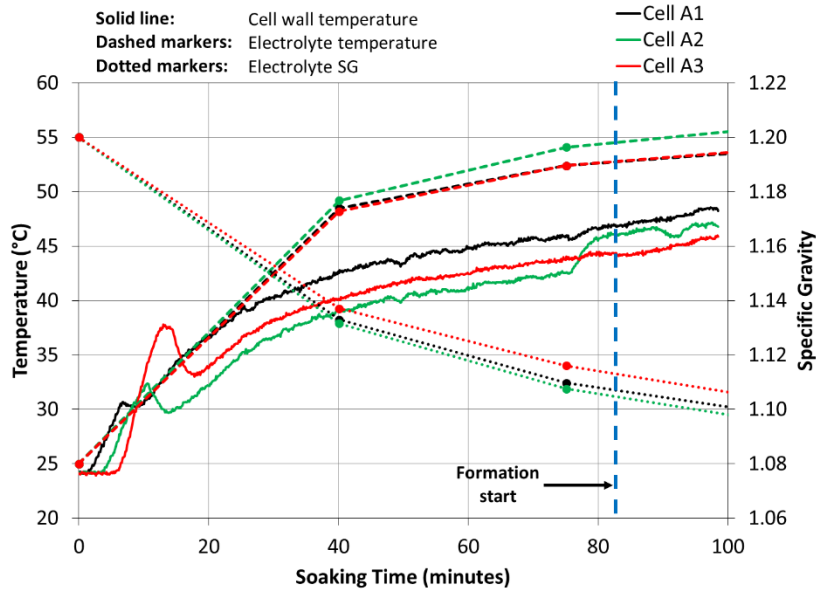
Figure 12   Soaking process of first three test cells (one 6 V module)

These trends were observed consistently in all test cells, although environmental conditions (e.g. room temperature, arrangement of adjacent cells, etc.) and cell dimensions did influence the peak soaking temperatures. It should be noted that the electrolyte was added on the basis of level and not volume. While there is slight variability in manufacturing that will affect the required volume to reach the desired level, any variations in filling volume were less than 3% from the average. The volumes of electrolyte added to each test cell before formation are provided in Table 8.

Table 8   Volume of 1.200 SG electrolyte added to cells

Cell ID	Volume (mL)	Cell ID	Volume (mL)
A1	3800	C1	5120
A2	3600	C2	5220
A3	3700	C3	5240
B1	3850	C4	5300
B2	3830	C5	5280
B3	3820	C6	5280
B4	3820	C7	5180
B5	3790		
B6	3820		
B7	3880		

4.2. Formation

Before discussing internal resistance results, it is necessary to establish the integrity of the formations themselves. To accomplish this, samples of the currents, voltages, temperatures, and SGs measured during formation data will now be presented and rationalized according to the presented scientific theory from Chapter 2.

The cell voltages obtained from each formation method are shown in Figure 13 with the corresponding currents. The voltages initially decrease before rising steeply and tapering off to a gentle upward slope. Note that cell A123 refers to the average cell voltage of the three 2 V cells in the 6 V module of set A. Cell B7 and cell C7 were chosen to represent their respective cell sets since they were the cells formed the longest. Since cell A123 and cell B7 have essentially the same specifications, it is clear that using a larger formation current results in a higher cell voltage. The progression of the cell C7 formation appears delayed compared to the others, which should be expected since it is a cell of larger capacity.
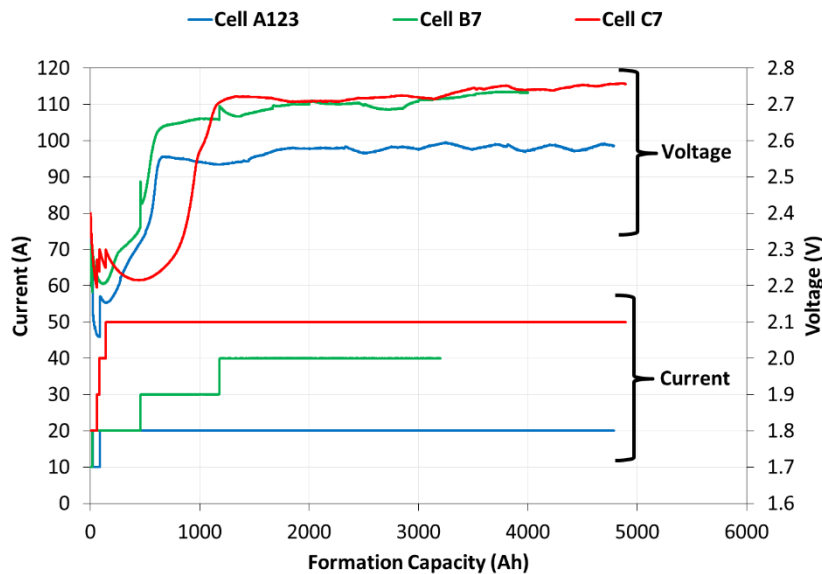

Figure 13   Currents and voltages during formations

To make a more level comparison of the different cell types, the abscissae must be scaled to the size of each cell. This is done using the PAM TC, which as the larger of the two electrode TCs can be treated as the TC of the full cell. Figure 14 shows the same voltages

as Figure 13, but plotted against the formation in terms of the percentage of the TC that has been applied, rather than the absolute Ah that have been applied. This technique will be used throughout this chapter. Figure 14 also shows the temperatures during the different formation techniques. Clearly, larger currents and voltages give rise to higher temperatures, as would be expected from Joule heating. The reverse influence of temperature on voltage is also obvious at higher formation levels, as otherwise-smooth voltage trends undergo small oscillations inverse to the cell temperature oscillations which occur on a daily cycle (due to ambient temperature variations). This effect comes from reaction kinetics, as higher temperatures allow the same current to flow with a lower overpotential, and expedite mass transport as well.
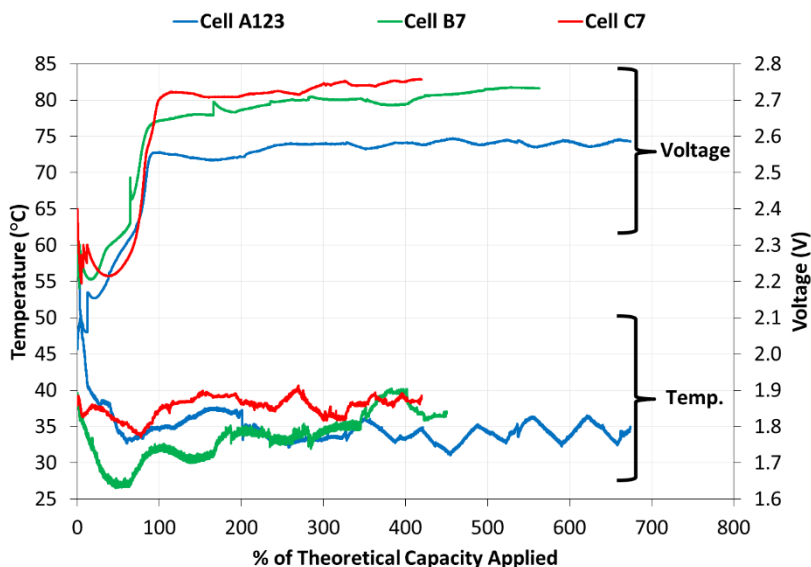

Figure 14 **Temperatures and voltages during formations with scaled abscissae**

Figure 15 provides a more detailed example of the varying cell characteristics during formation. For the cell shown, positive electrode potential (PEP) and negative electrode potential (NEP) half-cell voltages were measured with the reference electrode and the plate temperature was measured with the Teflon-coated thermocouple. As mentioned in Chapter 3, the current starts off at a relatively low value of 20 A to accommodate high soaking temperatures and low electrical conductivity of the unformed paste. The current is then gradually stepped up until a final value of 50 A is reached and held for the remainder of the formation.
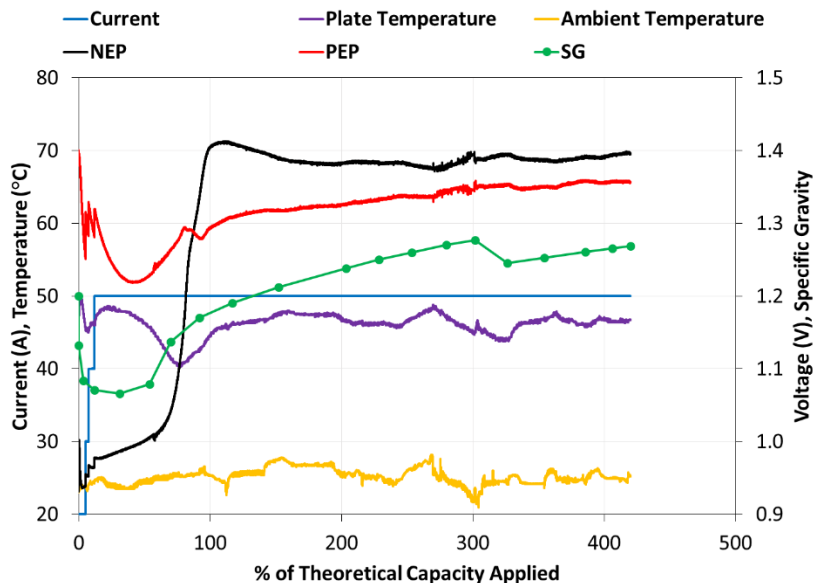
Figure 15   General cell characteristics during formation (cell C7)

The PEP starts at a relatively high value and declines to a minimum near the 40%TC mark before rising again. This is expected due to the two stages of formation described in Chapter 2. In comparison, the NEP starts at a much lower value, begins increasing much sooner, and reaches a higher value than the PEP after a sharp increase around the 100%TC mark. This is explained by the fact that the NAM has larger pores (as a result of the expander additive) as well as faster reactions than the PAM. These characteristics allow the NAM to charge at the same current as the PAM with a lower overpotential. Since the PEP is high at the beginning of formation, substantial O_2 gas evolution will proceed the entire time, while H_2 gas evolution will only become substantial after the large jump in NEP. Slight electrolyte bubbling was observed visually in the early stages of formation, which became much more prominent after the NEP jump.

The sharp rise in NEP is a result of the NAM charging so efficiently that the dissolved Pb^{2+} ions available for conversion to Pb are actually running out near the 80%TC mark. The NEP must then rise in order to maintain the same charging current, such that increased H_2 gas evolution is then carrying a significant portion of the total current. The flow of H_2 gas bubbles out of the NAM pores then forces much of the built-up H_2SO_4 reaction product into the bulk electrolyte.

Evidence of the clearing of H_2SO_4 from the pores into the bulk electrolyte is given in Figure 15 by a relatively sharp rise in SG around the same time as the voltage increase. Since the SG is measured at the top of the cell and not at the pores, the measured SG will underestimate the amount of SO_4^{2-} released from electrodes until either the acid diffuses naturally throughout the bulk electrolyte or until the intensive bubbling mixes the electrolyte and eliminates any gradients. The SG then continues to rise as a combined effect of the release of SO_4^{2-} from the electrodes and the removal of water through electrolysis. Eventually the water removal is significant enough that the electrolyte level has nearly fallen below the tip of the reference electrode, shown in Figure 15 by the slightly noisy behaviour of the NEP and PEP around 280%TC. The noisy behaviour is corrected by adding water to the cell, which is the proper practice to prevent the level from falling below the top of the plates as discussed in Chapter 3. The SG immediately drops as a result of the water addition, and then climbs again at approximately the same rate as before.

The plate temperature measured by the internal temperature probe is shown to be near 50 °C at the end of soaking. The temperature then decreases briefly as the cell naturally cools at low current values, and then increases again as the current is stepped up to 50 A. Next, the low voltage and endothermic behaviour of the formation cause the temperature to fall again until the sharp increase in both NEP and PEP cause an increase in Joule heating, resulting in another rise in temperature after 80%TC. After this point, the plate temperature mainly shows dependence on the ambient temperature, and the voltage shows slight variations inversely proportional to the variations in plate temperature.

These general formation characteristics represent all test cells, and these characteristics have been rationalized according to the presented scientific theory in Chapter 2. This necessarily establishes the integrity of the formations before considering the results specific to LAB internal resistance in the sections to come.

4.3.   Internal Resistance: Fast-response

In order to evaluate the ohmic component of the battery impedance throughout formation, fast-response results will first be examined. These results include AC injection, fast DC pulsing, and the built-in resistance-measuring function of the power-cycler. The theory

provided in Chapter 2 stated that during formation, the inactive nonconductive materials in the electrodes are being converted to conductive materials. At the same time, the electrolyte concentration (and thus, its conductivity) should reach a minimum in the early stages before increasing thereafter, and this was observed through manual SG measurements as shown previously in section 4.2. This means that the changing contributions of the electronic and ionic resistance to the overall ohmic resistance should oppose each other in the early stages of formation, but then combine constructively to decrease the ohmic resistance thereafter.

The first task is to compare the resistance measurements throughout formation given by the 16 millisecond pulses with those given by the built-in function running 1 millisecond pulses, as shown in Figure 16. The resistance generally decreases throughout formation in both cases, indicating that the decreasing electrode resistance must dominate the increasing electrolyte resistance in the first stage of formation. Considering that the bulk electrolyte SG is always maintained near the highly conductive range stated by Pavlov, while the electrode materials undergo a change in resistivity of several orders of magnitude, this result makes sense. Figure 16 also shows how the two instances of water addition indicated by the SG drops do not have an obvious impact on the measured resistance, further exemplifying the limited impact of the electrolyte on the changing ohmic resistance during formation.
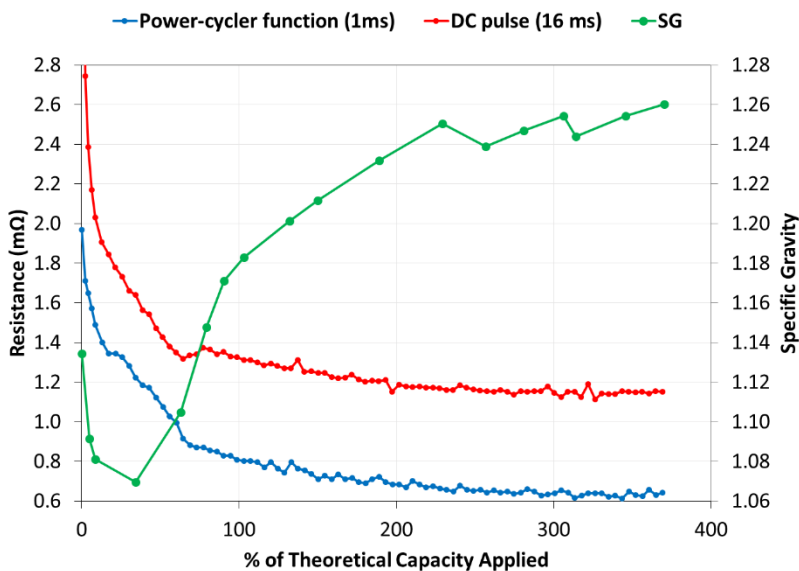

Figure 16   Results of DC fast-response methods (cell C6)

While the two trends in Figure 16 are quite similar, the longer pulse clearly captures more of a response than the shorter pulse, which should only occur if the EDL is participating. Figure 17 provides a closer look, revealing that while there is certainly some noise in the trends, both appear to be in a relative steady-state after applying roughly 280%TC. The sudden trend reversal in the 16 millisecond data near 60%TC is coincident with the sharp voltage increase experienced by the cell as the conversion of $PbSO_4$ to active materials slows down. This reversal is accentuated for longer pulse times, as will be shown later in section 4.4. The fact that this reversal is apparent in the 16 millisecond case but not in the 1 millisecond case suggest that the former includes some kinetic processes in the response, while the latter is more likely to only capture the ohmic response.
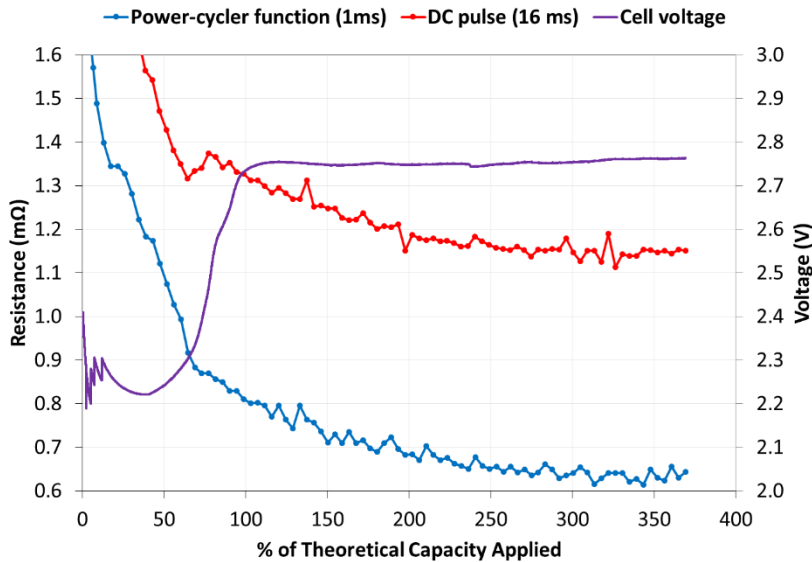

Figure 17   Zoomed-in comparison of DC fast-response results (cell C6)

Resistance measurements through AC injection were also obtained during the formation of the same cell. Figure 18 compares these manual measurements with the 1 millisecond results from the built-in function, showing that these two methods are in very good agreement. The similarities can be rationalized by considering that the handheld battery analyzer used for AC injection operates at 1 kHz, which of course corresponds to a period of 1 millisecond. Recalling that the built-in function uses 10 back-to-back pulses of 1 millisecond each, it makes sense that this method would approximate a 1 kHz AC signal. Since AC injection measurements were taken manually, this data is sparser and appears as

a cleaner trend that may just be reaching steady state between 300%TC and 350%TC. Figure 18 also illustrates how the small fluctuations in the measured ohmic resistance do not directly coincide with the fluctuations in cell temperature. This may indicate that the slope of the resistance trend at higher formation levels is shallow enough that the measurement resolution becomes a factor.

It can be concluded that for fast-response resistance, both DC and AC methods can be successfully employed to measure the ohmic response of a LAB. Since the observed trends fit with theoretical expectations, the relative steady-state seen near 300%TC could be an indicator that no measureable amount of material is being converted at the electrodes beyond this point in the formation.
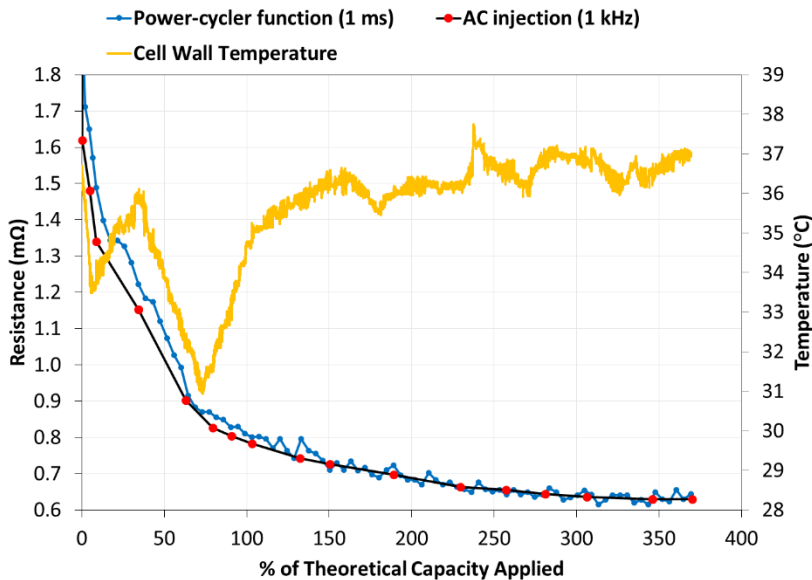

Figure 18   Comparison of fast-response resistance methods (cell C6)

4.4.   Internal Resistance: Slow-response

The first experiment with cell set A employed both a pulse-up technique and a pulse-down technique to explore internal resistance measured with 10-second pulses during a 20 A formation. The results obtained from both techniques for all three A cells are given in Figure 19 and Figure 20. Firstly, comparing the three individual cells shows that they are in very close agreement with each other throughout the formation, indicating high repeatability of the results. The trends themselves start with a decrease and end with a slow

decay just as the fast-response trends did, but the slow responses show a large bump between 25%TC and 100%TC. Furthermore, there is a substantial difference in the size and shape of the bump when comparing pulse-down to pulse-up.
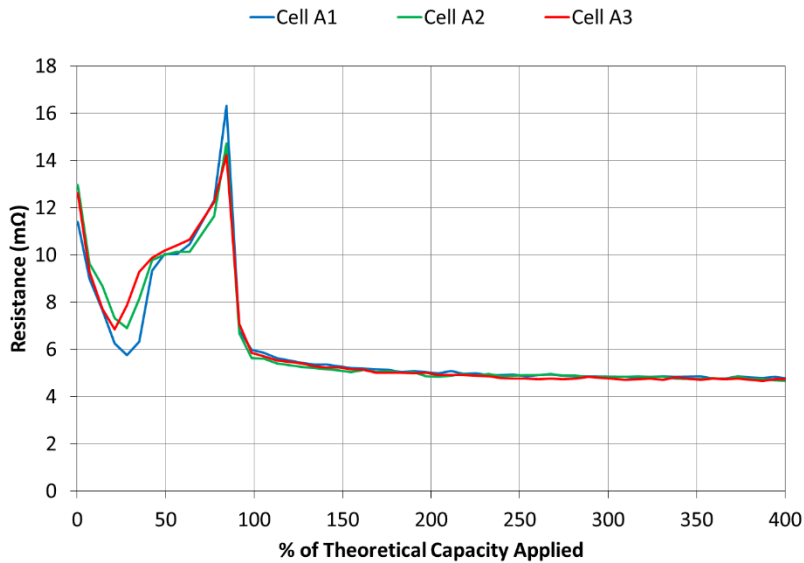

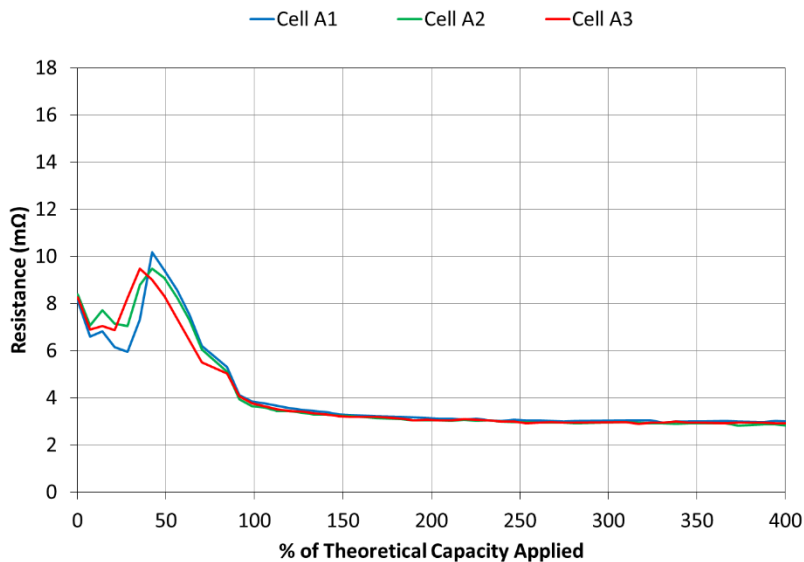**Figure 19   10-sec DC pulse-down resistance (cell set A)**

Figure 20   10-sec DC pulse-up resistance (cell set A)

In order to explain these seemingly abnormal results, the Butler-Volmer equation must be revisited. Figure 21 shows six plots intended to represent the kinetic responses to a pulse-down and a pulse-up at six different points in a LAB formation (or any charge). Butler-

Volmer equations were created to describe both the main conversion reaction and the electrolysis side reaction, with the total faradaic current representing the sum of the two. The dashed blue lines intersect at the operating points of the total current and corresponding overpotential for states of base, pulse-up, and pulse-down. The only variable in Eq. (9) that changes from one plot to the next is the area term, where the sum of the conversion reacting area and the electrolysis reacting area is constant. So, in the beginning of the charge when only 1% of the inactive surface area has been converted, 99% of the total area is available for the conversion reaction and 1% is available for the electrolysis reaction. The two areas trend in opposite directions until their values are reversed at the end of the charge. Note that these curves were developed purely for illustrative purposes and do not necessarily resemble a physical system.
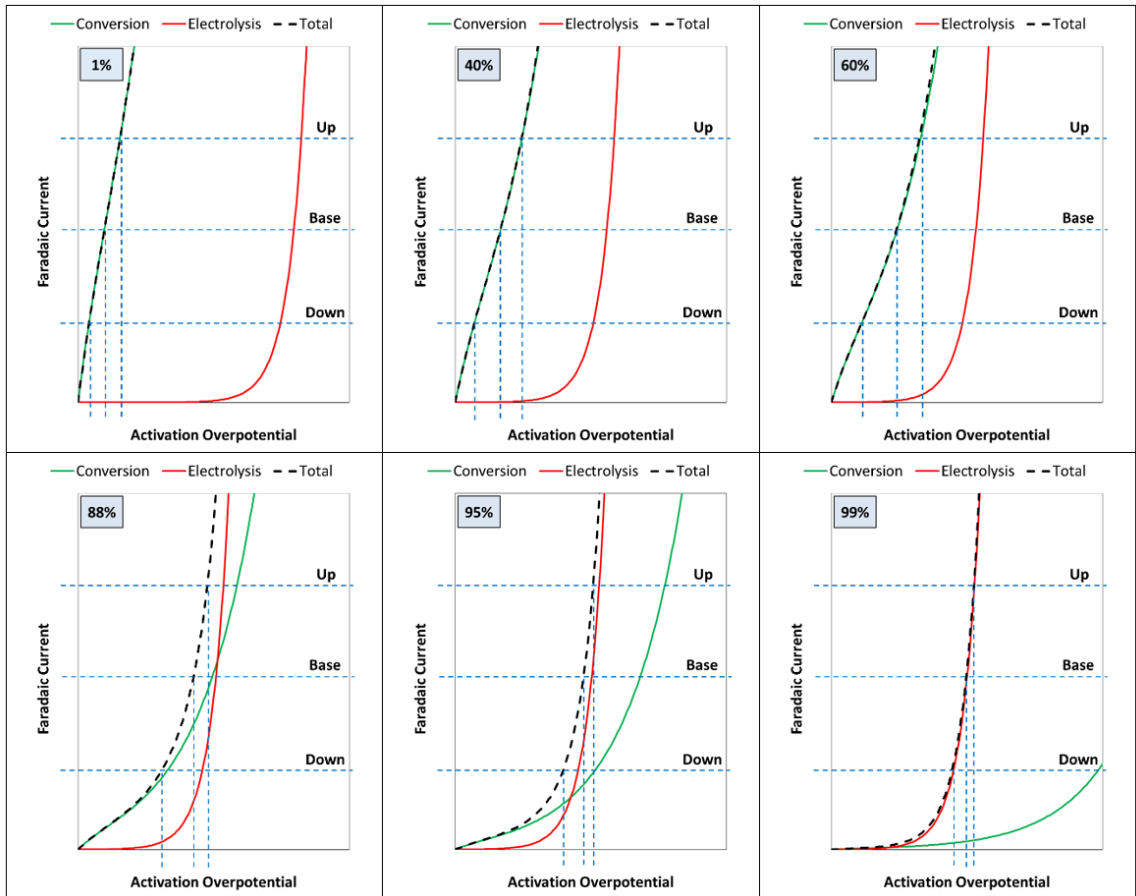

Figure 21   Slow-response trends explained through Butler-Volmer

At 1% area conversion, the low overpotential of the main reaction allows the base current to flow at a low voltage. Pulsing the current in either direction causes a small voltage change due to the steep slope of the curve. The high overpotential for electrolysis results in virtually all of the total current flowing through the main reaction. As the available area for the main conversion reaction declines, the slope of the conversion curve decreases, such that the voltage must increase to hold the same base current and pulsing in either direction requires a larger voltage change than it did previously.

A transition period exists near 88% conversion, where the base current is being met partially by electrolysis. Pulsing down nearly erases the need for electrolysis, while pulsing up increases the current mainly through the steep electrolysis curve. As a result, the required voltage change for a pulse-up begins to shrink while that for a pulse-down remains large. At 95% conversion, most of the total current is flowing through electrolysis, such that pulsing in either direction follows a steep slope. Now the voltage change for a pulse down begins to shrink as well. Thereafter as less and less area becomes available for the main conversion reaction, the total current becomes more and more in line with the steep electrolysis curve. Thus, the voltage change required for a current pulse in either direction becomes smaller and smaller as the area conversion nears 100%.

This explanation illustrates just how crucial the Butler-Volmer equation is to understanding how slow-pulsing evolves throughout a charge or formation. To verify that these concepts do in fact apply to the present experimental data, the actual 10-second pulse responses from cell set A will now be explored more closely. For simplicity, the three individual cells A1, A2, and A3 have again been lumped together as A123 for this analysis.

Figure 22 shows the profiles of the voltage response to the current pulses throughout the bump region of Figure 19 and Figure 20. Recall that during the pulses data is recorded every 16 milliseconds, and outside the pulses data is recorded every 6 seconds. Thus the linear climb at the end of the pulse is actually just a jump to the next data point 6 seconds later, shown as broken lines for clarity. At 35%TC the base voltage is low, indicating that the current is mostly going through the main reactions. When the current is suddenly reduced, there is an immediate ohmic change and the required activation overpotential is

reduced according to Butler-Volmer. The EDL self-discharges through the main reactions and approaches a new equilibrium which is not quite reached in the ten seconds allotted. At 56%TC and 77%TC, the available area for the main reactions have decreased and thus the overpotential has increased to maintain the base current. Pulsing down now requires a larger voltage drop, as predicted in Figure 21. At 85%TC the cell is likely in a transition region such as the 88% conversion plot in Figure 21. The high base voltage indicates that the cell is likely gassing significantly, but the suddenly reduced current does not require a contribution from electrolysis, and the corresponding voltage drop is at its largest. At 92%TC, both the base current and the reduced current require intensive electrolysis, and the steepness of the current-voltage relationship in this region reduces the voltage drop when the current is pulsed down. At 99%TC, the voltage drop decreases even more as the available area for electrolysis gradually increases.

Figure 23 shows the equivalent data for pulsing up, for which the same principles apply. The key difference is that the voltage spikes decrease in magnitude earlier than in the case of pulsing down, as predicted in Figure 21. Figure 24 and Figure 25 highlight the later stages of formation when the evolution of the pulse response is much more gradual. Note that the base voltages have all been set to zero in these figures for convenient comparison. While the difference from one pulse to the next is very slight, there is still a measurable change, which means there is a measurable change in the amount of material that has been converted.
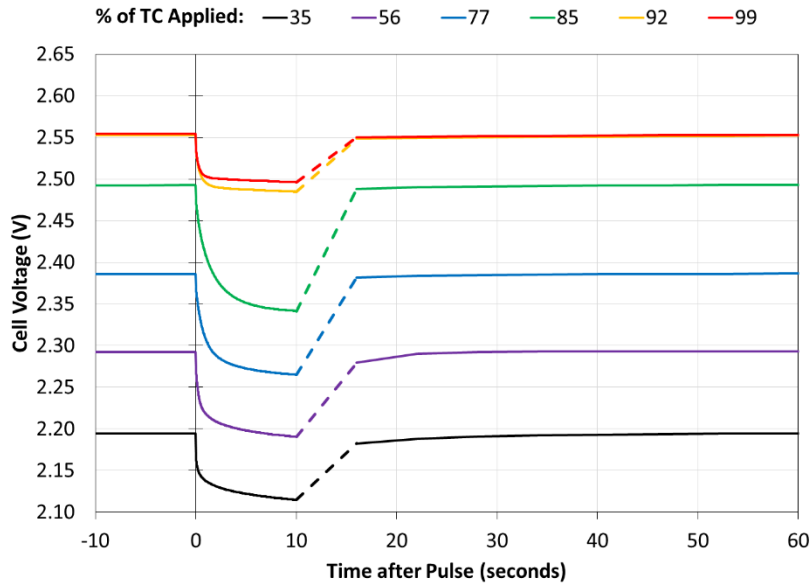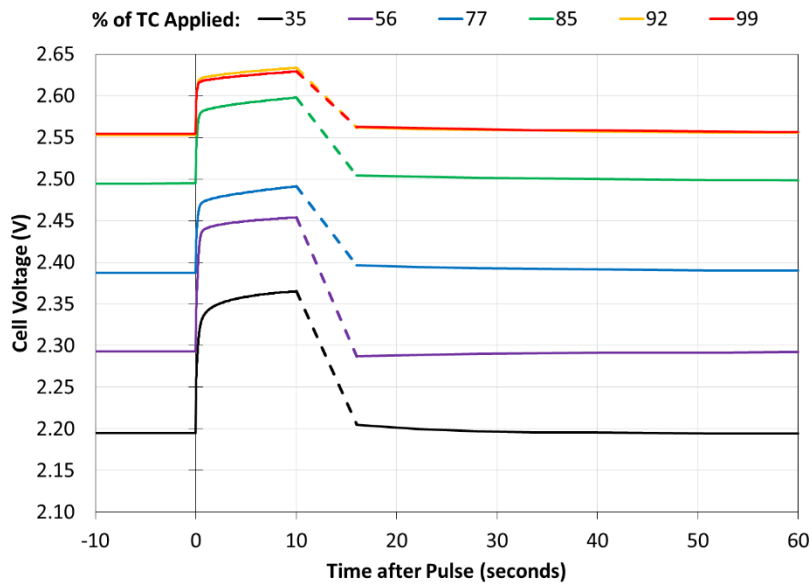
Figure 22   Early slow-response of pulse-down (cell A123)
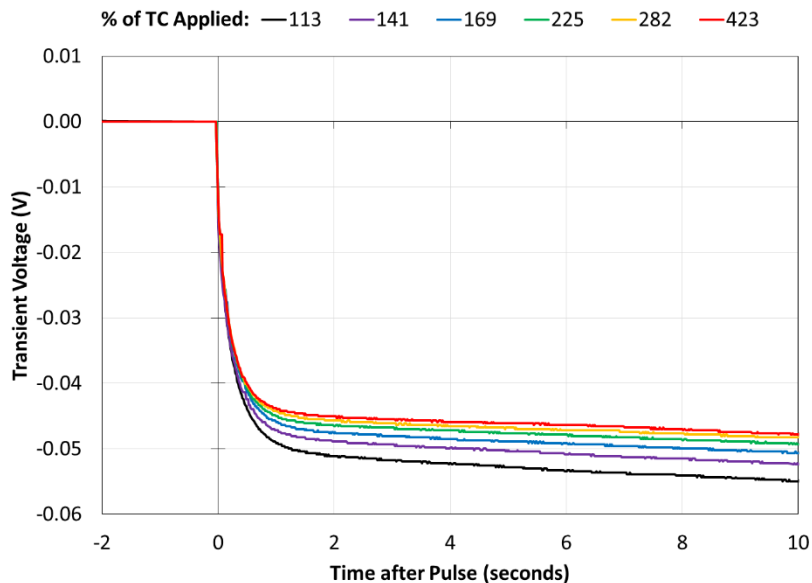

Figure 23   Early slow-response of pulse-up (cell A123)

Figure 24   Late slow-response of pulse-down (cell A123)
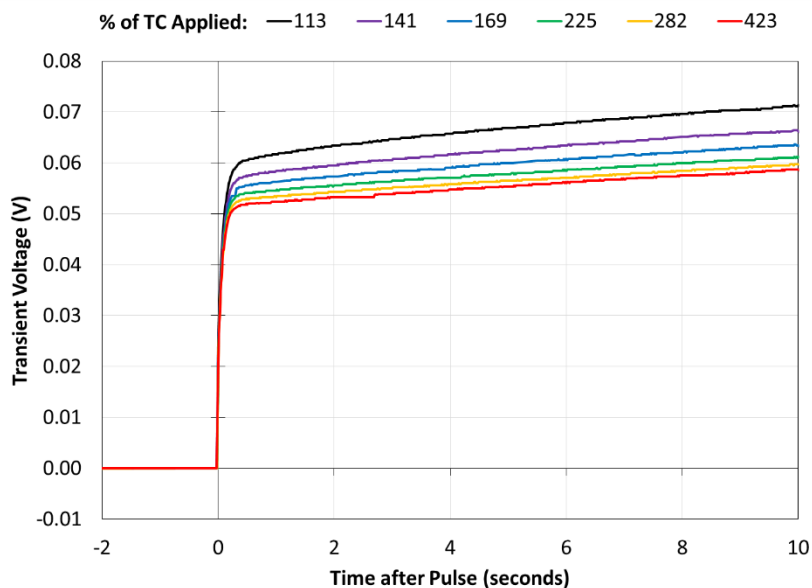
Figure 25   Late slow-response of pulse-up (cell A123)

Figure 26 focuses on the region of Figure 19 and Figure 20 pertaining to these later formation stages. Both trends indicate that a relatively steady state is reached around 350%TC. According to the concepts just discussed, the steady state may indicate that continuing the formation beyond this point would yield little extra material conversion. Figure 26 also indicates that while the pulse up resistance is smaller than the pulse down resistance, it appears to be a cleaner trend, although this may be related to the fact that the

pulse magnitude was greater. Even so, upward pulses were the focus of subsequent experiments in the laboratory.
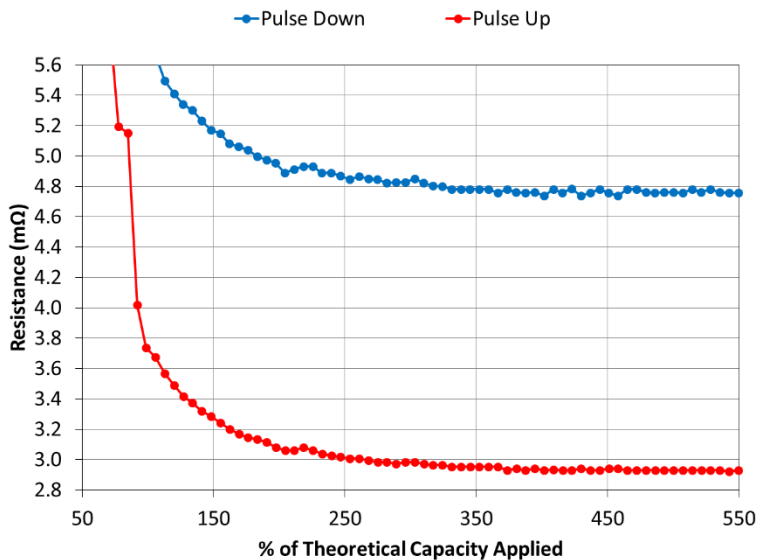

Figure 26   Slow-responses approaching steady-state (cell A123)

In order to investigate the contributions of both electrodes to the total resistance during formation, cell C6 was later formed with upward 10-second pulses while making use of the reference electrode. The results of this experiment are presented in Figure 27. The trends show that the positive electrode resistance is almost always decreasing, while the negative electrode resistance features the large valley and peak that are observed in the full cell resistance. By 150%TC, the negative electrode resistance has stopped changing significantly, while the positive electrode resistance continues to decline up to 300%TC. This is a likely indication that the NAM is completely formed much earlier than the PAM, as would be expected due to the lower TC of the NAM and also due to the higher formation efficiency of the NAM discussed previously. Thus, the long decay in the total resistance is a result of greater formation requirements in the PAM.
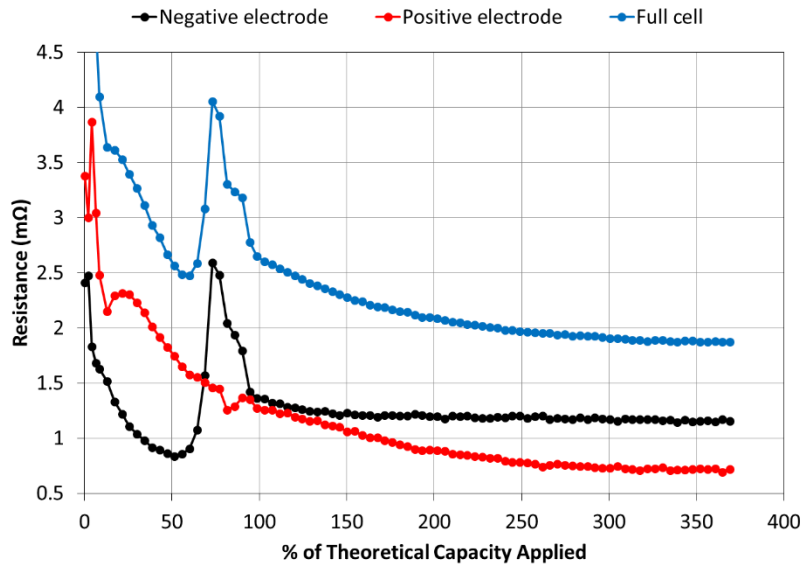
Figure 27   **Half-cell 10-sec DC resistance trends during formation (cell C6)**

4.5. Correlating Internal Resistance and Formation Completeness

Internal resistance measurements were taken during additional formations, this time with the intention of correlating the resistance trends to the completeness of the formation. As discussed in Chapter 3, seven cells of set B were formed to different levels with upward pulses, and the test was repeated on seven cells of set C.

4.5.1. Group Formations

Figure 28 and Figure 29 show the results of the B formation, while Figure 30 and Figure 31 show the results of the C formation. Both datasets exhibit the decrease-bump-decay trend observed previously, with key differences coming from the fact that the B cells were formed at current steps while the C cells were formed almost entirely at constant current. Referring again to Butler-Volmer, the sudden drop in resistance near 170%TC for the B cells can be explained by the increase in base current at the same instance. Pulsing up from a higher base current makes the current follow a steeper slope on the exponential Butler-Volmer curve, so the resistance should be expected to drop. Despite this discontinuity, the decay trend continues throughout the rest of the formation.
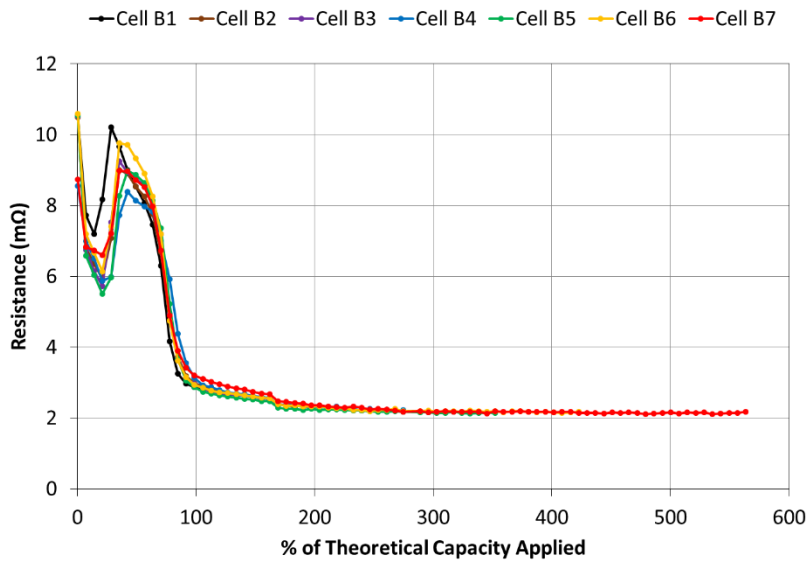
Figure 28   **10-sec DC resistance trends during formation of set B cells**
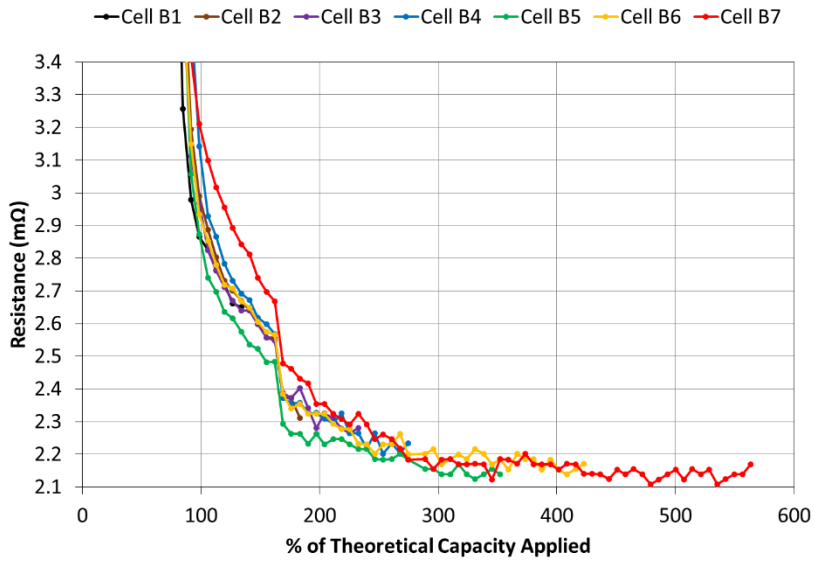
Figure 29   **10-sec DC resistance trends of set B cells (zoomed)**

60
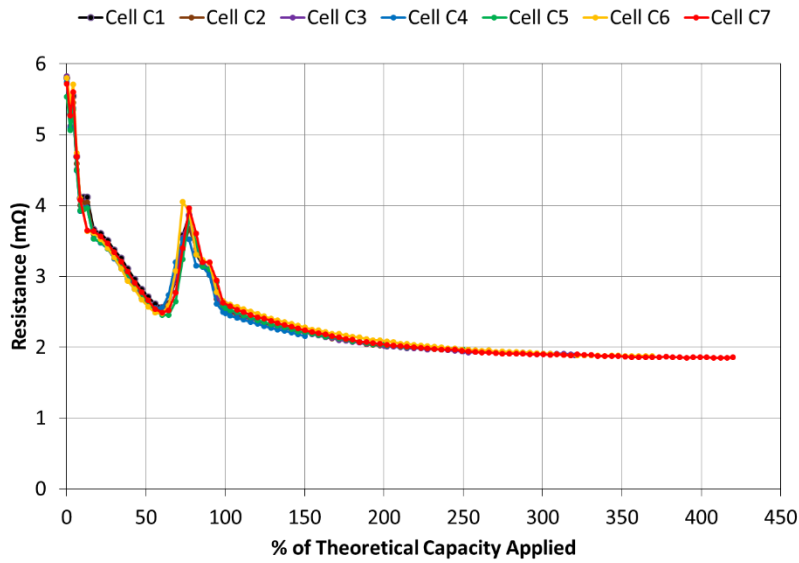
Figure 30   10-sec DC resistance trends during formation of set C cells
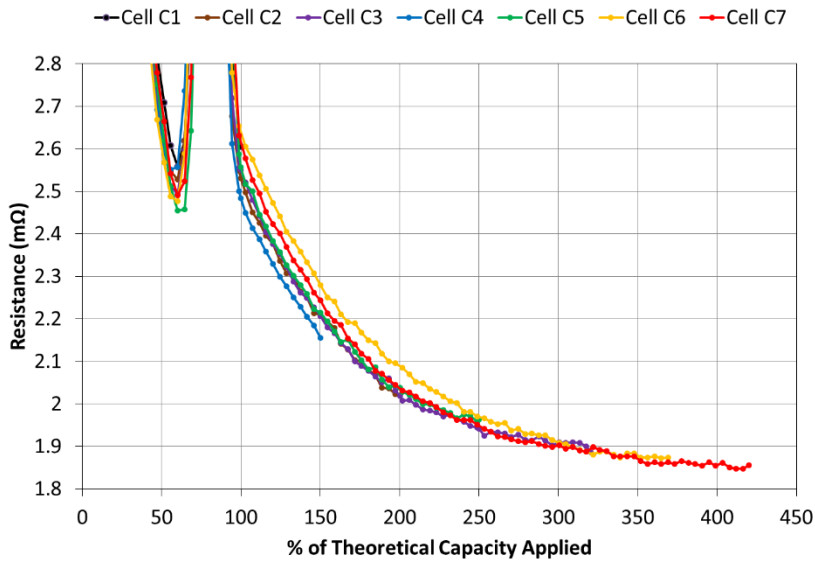
Figure 31   10-sec DC resistance trends of set C cells (zoomed)

It is important to realize that the slow-response actually includes the fast-response, i.e. it has both ohmic and kinetic components. Since smooth ohmic resistance trends were obtained for cell C6 with the manual AC injection measurements, this data was used to illustrate the composition of the slow-response. The sparse AC injection data was interpolated such that there was a value of ohmic resistance to coincide with every DC pulse during the formation of cell C6. Then, the ohmic resistance was subtracted from the

total slow-response resistance to approximate the kinetic resistance. Note that the kinetic resistance is not necessarily equivalent with the charge-transfer resistance, as the charge-transfer resistance may not be measured accurately due to the capacitance of the EDL. The kinetic resistance can be considered as the non-ohmic resistance that is captured in the given time frame, which in this case is 10 seconds.

Figure 32 illustrates the relative magnitudes of these resistance components, noting that the magnitude of the kinetic resistance will increase with the duration of the pulse since the voltage will typically continue to change if more time is given for the EDL to charge. In Figure 33, the three curves have been offset such that their respective minimum values are all equal to zero. This reveals how the slope of the kinetic trend is much greater than that of the ohmic trend, and will therefore have better sensitivity as the formation nears its end. The total resistance combines both of these, giving it the greatest slope. Thus even though a fast-response trend and a slow-response trend may reach a relative steady state at the same time, the slow-response trend would be expected to have much better sensitivity as it does so.
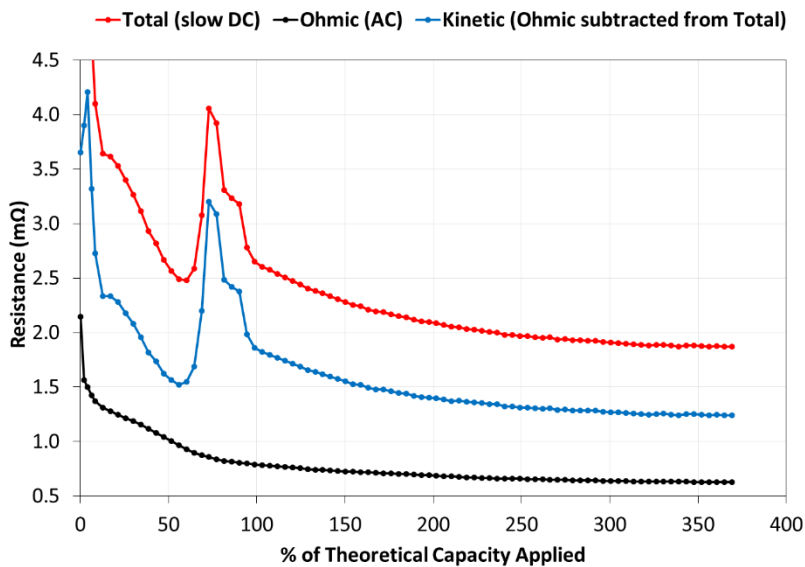
Figure 32   Ohmic, kinetic, and total resistance (cell C6)
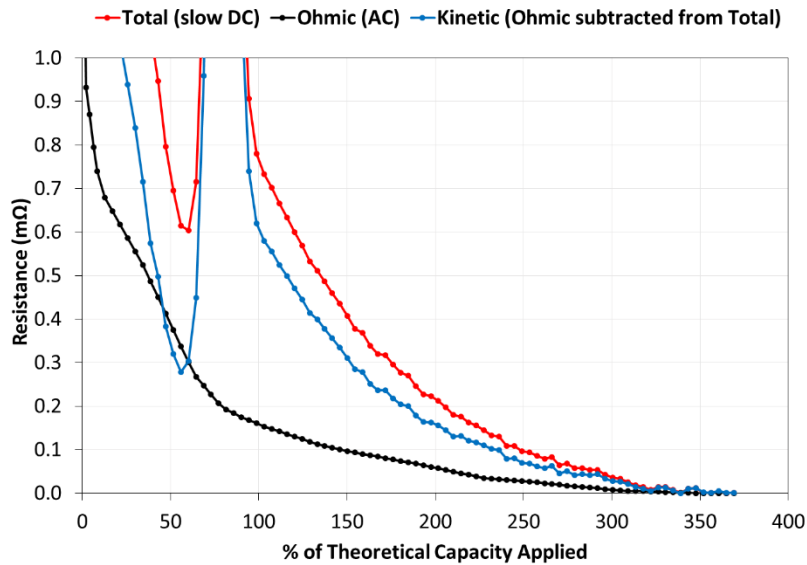
Figure 33   Ohmic, kinetic, and total resistance (cell C6) (zoomed)

4.5.2.   Discharge Tests

After the cells were formed to their desired levels, their capacity was tested through a C/4 rate discharge test. The results for each cell are listed in Table 9, where discharge capacities are corrected to 25 °C as per Eq. (21). According to the cell specifications in Appendix A, the C/4 rated capacities for set B and set C are 244 Ah and 296 Ah, respectively. These capacities should technically be de-rated for electrolyte SGs lower than the 1.280 SG specified in the data sheets, but since cells were formed to different levels thereby achieving different SGs anyway, the specified discharge ratings are upheld in this analysis for the sake of comparison.

Table 9   **Summary of capacity inputs and outputs**

Cell ID	Formation Capacity Applied (Ah)	% of Theoretical Capacity Applied	Capacity Discharged (Ah)	% of Rated Capacity Discharged
B1	1000	141	117	48
B2	1333	188	176	72
B3	1667	235	215	88
B4	2000	282	223	91
B5	2500	352	238	97
B6	3000	423	249	102
B7	4000	563	255	105
C1	1166	100	67	23
C2	1751	150	128	43
C3	2334	200	174	59
C4	2913	250	222	75
C5	3733	320	263	89
C6	4315	370	261	88
C7	4894	420	264	89

The discharge curves for the B cells are shown in Figure 34, and the resulting discharge capacities are plotted with the corresponding formation input in Figure 35. Of course, greater formation capacities correspond to greater discharge capacities, but it can be seen that any extra input almost always yields diminishing extra output. The cell formed to 235%TC appears to obstruct this trend, but Table 10 explains why this is the case. As stated in Chapter 3, whenever a cell had formed to the desired level and was left to rest, the electrolyte was topped with 1.265 SG electrolyte to an approximate final height recommended by SBCL Following this method strictly resulted in the 235%TC cell receiving an abnormally high volume of extra electrolyte (shown in red) when compared to the other cells. Since higher acid concentration will reduce the voltage drops in the cell during discharge, the extra electrolyte addition manifests as a slightly inflated discharge capacity. It is also important to note that the three highest formation levels all surpassed 97% of the rated C/4 capacity despite having lower SGs than the specification, indicating that the cells were well-formed by the manufacturer's standards.
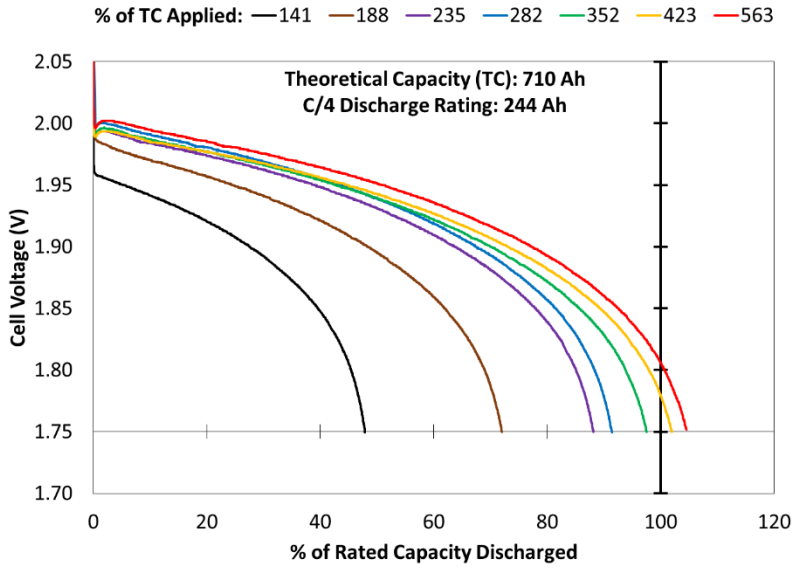
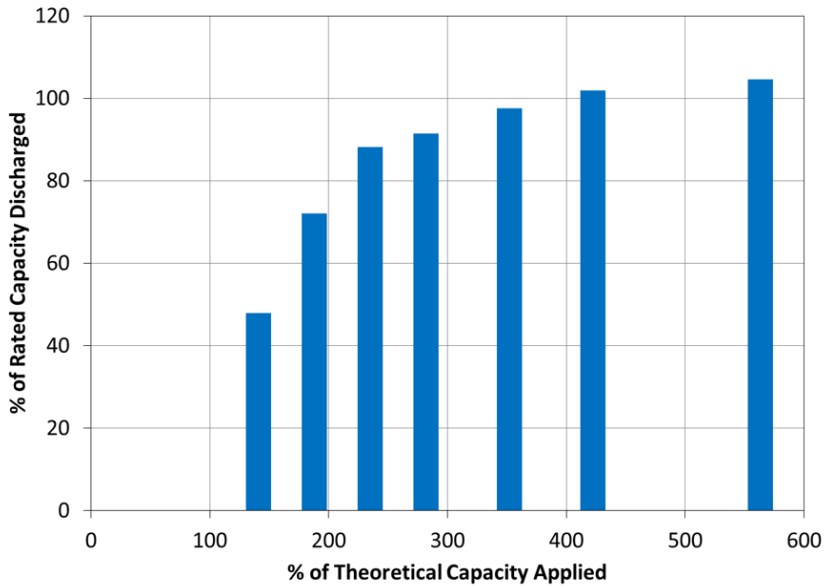**Figure 34**   Voltage curves on during C/4 discharge (B cells)

Figure 35   Discharge capacity plotted against formation capacity (B cells)

Table 10   End-of-formation summary (B cells)

Cell ID	% of Theoretical Capacity Applied	mL of water added while forming	mL of 1.265 SG electrolyte added after forming	Final SG after forming	Final EMF after forming
B1	141	0	490	1.2024	2.053
B2	188	0	590	1.2263	2.079
B3	235	0	**920**	1.2410	2.089
B4	282	0	740	1.2487	2.095
B5	352	500	570	1.2420	2.090
B6	423	500	680	1.2484	2.085
B7	563	750	700	1.2568	2.103

The same series of results given for set B are now given for set C in Figure 36 and Figure 37. As with set B, there is diminishing extra discharge output with extra formation input, and one cell (the 320%TC cell in this case) appears to be a slight outlier. Table 11 shows how this cell likely achieved a slightly inflated discharge capacity as a result of the amount of electrolyte added to it post-formation (shown in red) in comparison with the cells that followed it. During formation, water is added to the cells when necessary, but in the case of the 320%TC cell, it had just finished forming at the point when it would have needed water. Thus, the cell was topped up entirely with 1.265 SG acid, when it may have been more appropriate to use water for perhaps half this volume. The same argument could be made for any cell that did not receive water during formation, but the effects are certainly most pronounced on the 320%TC cell. Clearly the 1.265 SG electrolyte addition does factor into the discharge performance of the battery and should have been taken into more careful consideration when topping up the formed cells. Even so, the observed effects were slight and do not decrease the value of the trend analysis.
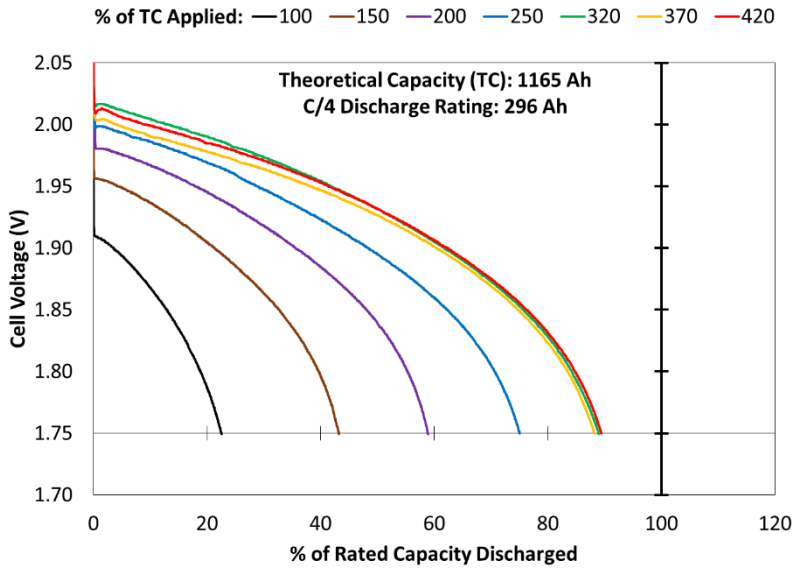
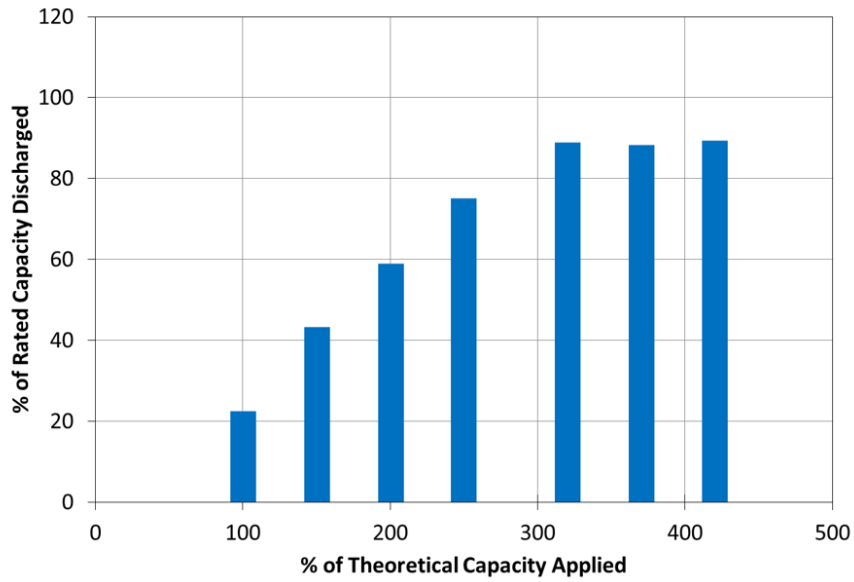**Figure 36   Voltage curves on during C/4 discharge (C cells)**

Figure 37   Discharge capacity plotted against formation capacity (C cells)

Table 11   End-of-formation summary (C cells)

Cell ID	% of Theoretical Capacity Applied	mL of water added while forming	mL of 1.265 SG electrolyte added after forming	Final SG after forming	Final EMF after forming
C1	100	0	600	1.1777	2.036
C2	150	0	600	1.2202	2.068
C3	200	0	700	1.2427	2.091
C4	250	0	900	1.2611	2.109
C5	320	0	**1100**	1.2733	2.130
C6	370	640	500	1.2592	2.112
C7	420	800	900	1.2672	2.119

Given the similarities between the B cell trends and C cell trends, it is expected that the proposed method should apply to all similar cell types. It is important to note however that while the discharge capacities of the well-formed B cells met their specified manufacturer rating, none of the C cells met theirs (up to 89%). Apart from the effect of cells having lower SGs than the 1.280 in the cell specifications, this is likely due in part to the greater plate thickness of the C cells, which are typically formed by SBCL using a mid-formation discharge. This technique was discussed in Chapter 2 and is done to enable the conversion of otherwise-inaccessible inactive material deep inside the plates. To explore this further, cell C6 was deep-cycled for an additional 17 cycles with an average overcharge of 15%. Figure 38 shows how the capacity increases greatly through continued cycling. This however does not negate the benefit of using a termination indicator during formation. The discharge capacity of cell C6 on cycle 19 would never be attainable on cycle 1, and a termination indicator would simply indicate when the formation is no longer making a valuable contribution to that first discharge. As discussed in Chapter 2, some inactive material can only be converted through continued cycling, regardless of the formation.
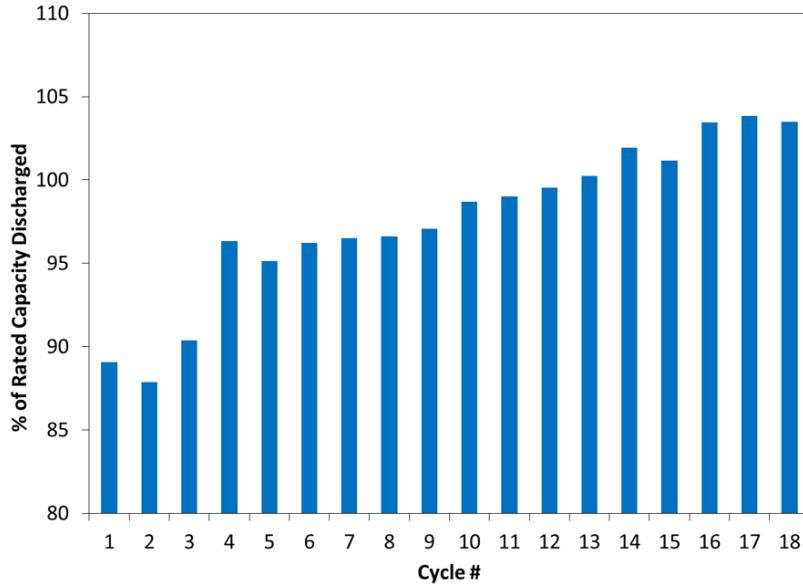
Figure 38   Continued deep-cycling of cell C6

4.5.3.   Differential Resistance

Rather than visually attempting to determine when a resistance trend has reached a relatively steady state for comparison to discharge capacities, the differential resistance was ultimately used as the indicator, as calculated per Eq. (20) which is restated here for convenience:

$$DR_j = \frac{IR_j - IR_{j-x}}{Cap_j - Cap_{j-x}} \tag{20}$$

Figure 39 and Figure 40 compare the differential resistance to the original slow-response resistance for the B cells and C cells, respectively, where the number of pulse intervals between the two points in the calculation, x, is taken as 1. The original resistance is presented as an average of the seven cells being formed, so as the formation proceeds, fewer cells are included in the average. This manifests as an increasingly noisy resistance trend at higher formation levels. The discontinuity at 170%TC in Figure 39 is minor in the differential resistance trend, indicating that this method should be able to accommodate changes in formation current. Since the experiment with the C cells made use of back-to-back pulsing, the average resistance and differential resistance appear much less noisy for this cell set.
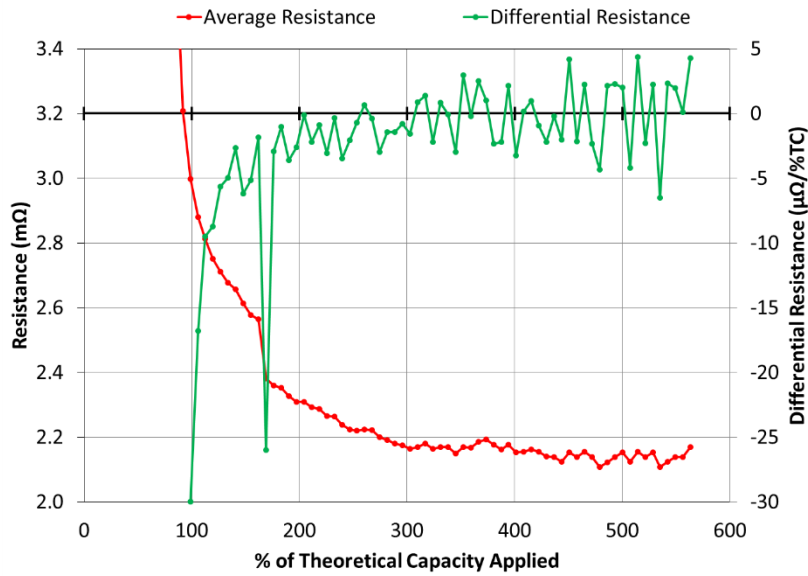
Figure 39   Differential resistance trend (B cells)
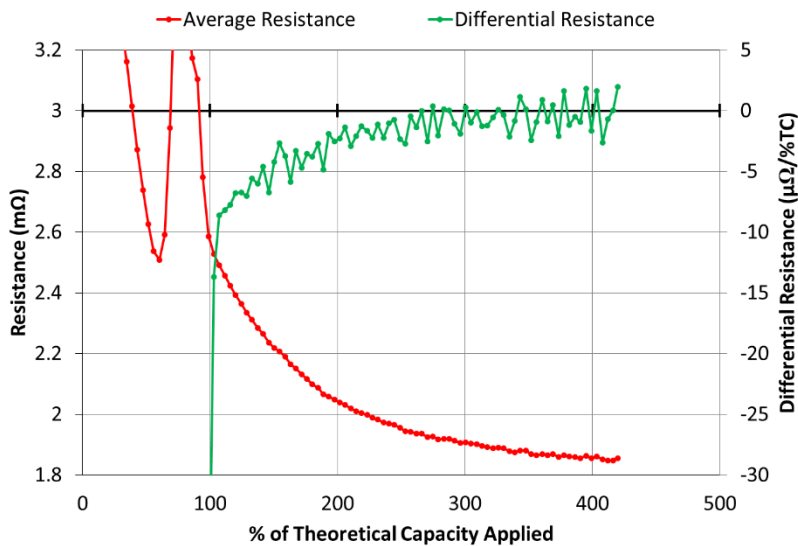
Figure 40   Differential resistance trend (C cells)

By employing Eq. (20) with higher values of x (more pulsing intervals between the two points taken into the calculation), the noise in the differential resistance is reduced, as shown in Figure 41 and Figure 42. Thus, the value of x acts as a filtering mechanism, and in general, this results in the differential resistance trend crossing the zero line at higher formation levels for larger values of x.

70
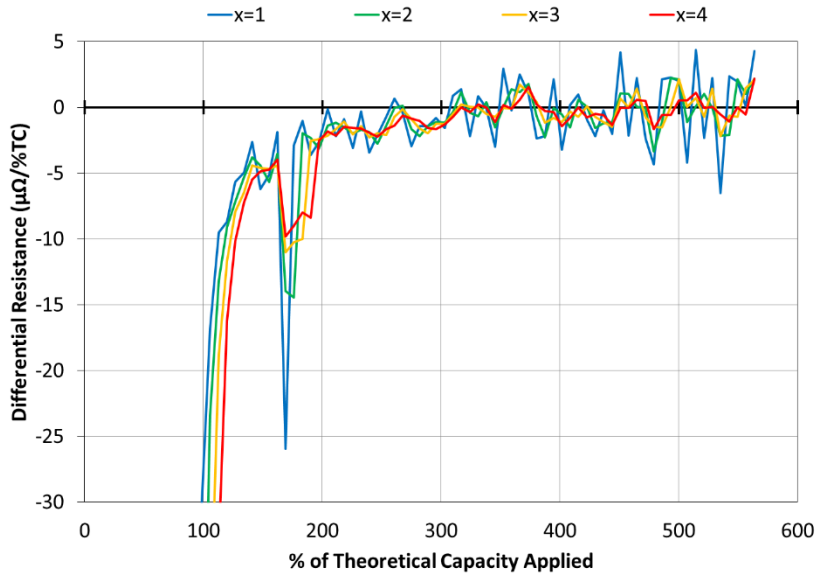
Figure 41   Differential resistance for different values of *x* (B cells)
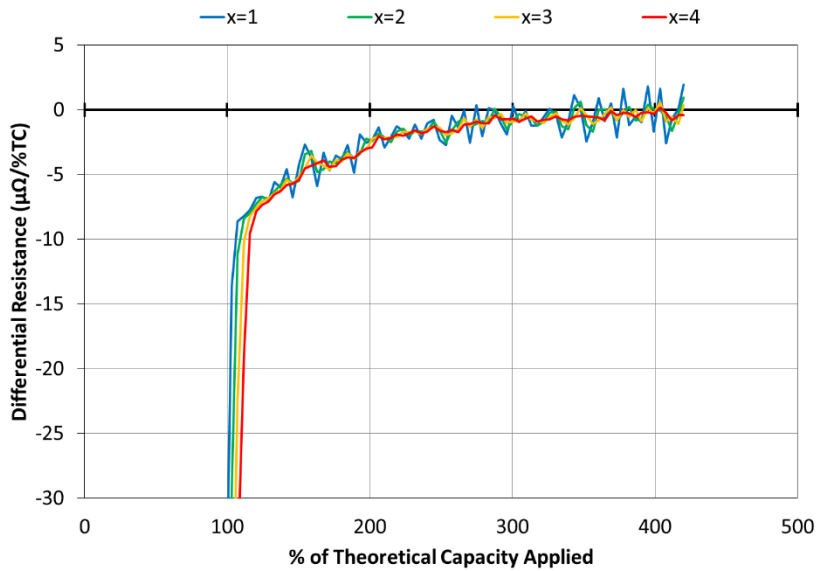
Figure 42   Differential resistance for different values of *x* (C cells)

Finally, the differential resistance trends are plotted together with the discharged capacities for the B cells in Figure 43 and the C cells in Figure 44. In both figures, the differential resistance is shown both with $x = 1$ and with $x = 4$, and in the case of the B cells a 5-point moving average is applied to the latter for additional filtering. For the B cells, it can be seen that while the trend is noisy, the average crosses the zero line around 350%TC and fluctuates about zero thereafter. Considering the relatively small amount of additional

discharge capacity gained through additional formation after this point, the point at which the differential resistance reaches zero appears to be a strong indicator of when the formation should be considered complete.
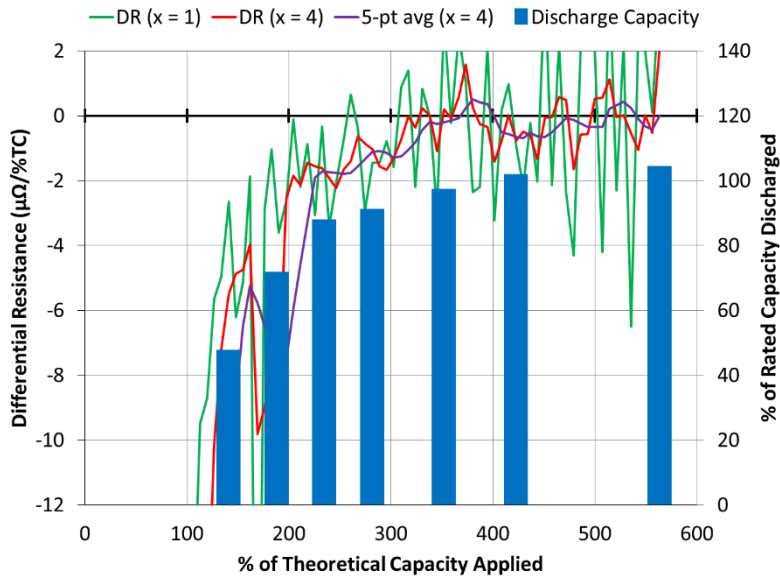
Figure 43   Termination indicator during formation (B cells)

For the C cells in Figure 44, the relatively clean resistance trend from the back-to-back pulses results in the differential resistance trend having little noise when $x = 4$, so no additional filtering through a moving average is required. In the $x = 4$ case, the trend follows the discharge capacity curve almost exactly (keeping in mind that the discharge capacity at 320%TC is slightly inflated due to the disproportionate electrolyte addition). The differential resistance curve does not cross the zero line until about 400%TC, when the discharge curve is essentially flat. While this does effectively indicate a more complete formation, the input capacity spent between 300%TC and 400%TC is enormous compared to the additional discharge capacity that was gained during this time. It should be considered though, that this additional discharge capacity may be much more relevant when the batteries are discharged at very low current rates, such as would be seen in an off-grid solar application. This is one recommendation as an area of future research.
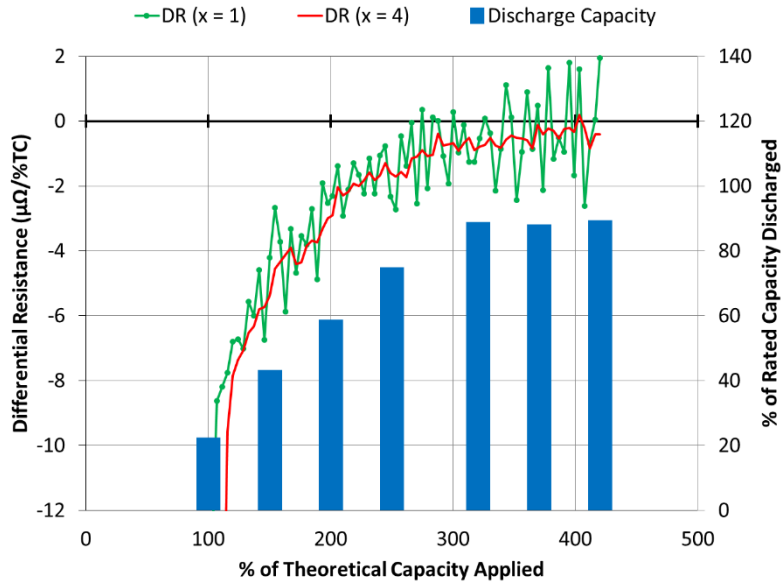
Figure 44   **Termination indicator during formation (C cells)**

In cases when the small additional discharge capacity is undesirable, the unfiltered differential resistance trend ($x = 1$) may actually be a more practical termination indicator than the filtered one. Such a strategy could potentially count the number of zero crossings that occur and terminate once a set limit is reached. In Figure 44, this might result in a termination closer to 300%TC, which would likely be considered more practical to most LAB manufacturers. In theory, a manufacturer employing the differential resistance method might even tune the level of filtering applied to the trend based on the needs of the customers, such that a course filter permits the formation to terminate a little early, while a fine filter forces the formation to a more completed state.

The differential resistance method was also applied to the fast-response resistance data. Figure 45 shows the results for the 1 millisecond DC ohmic resistance measured by the power-cycler built-in function. For $x = 1$, the differential resistance is already crossing zero near 100%TC due to the very small changes in the resistance from one point to the next. Only after the 5-point moving average is applied to the $x = 4$ case does the trend show substantial improvement, where the termination point appears to be around 280%TC. Even in this case, the trend is always much closer to the zero line in comparison to the slow-response trends, making it more difficult to interpret with confidence. This result is due to the fact that the fast-response resistance trend is less sensitive than the slow-response

resistance trends, as discussed in subsection 4.5.1. It is noteworthy however that the slow-response resistance trends were an average of seven cells, whereas reliable DC ohmic data could only be obtained when running the formation on a single cell, which was the case for the data shown in Figure 45.

Figure 46 shows the differential resistance for the 1 kHz ohmic resistance measured manually by the handheld battery analyzer. Since there are far fewer data points in this trend than in those previously discussed, it is relatively easy to interpret. The only zero crossing occurs on the last data point near 370%TC, which is near the termination point indicated by the slow-response trend of the C cells (Figure 44).
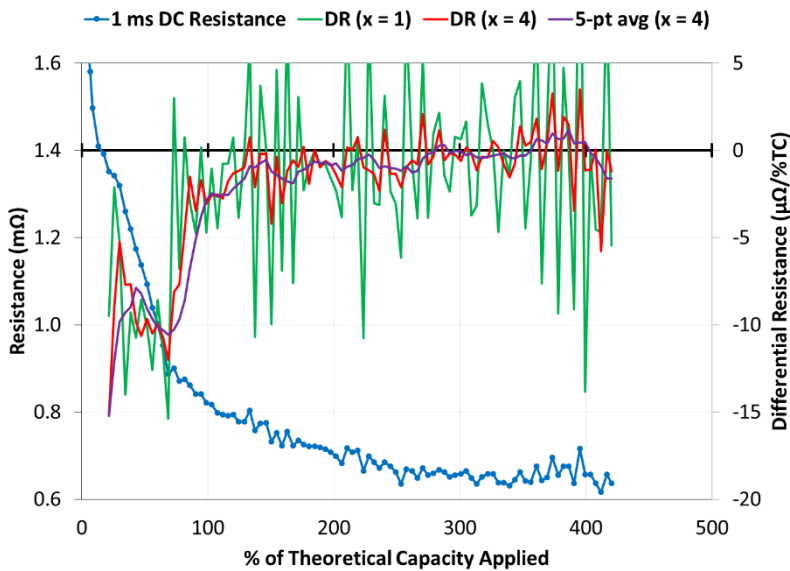
Figure 45 **Differential DC ohmic resistance as termination indicator (Cell C6)**
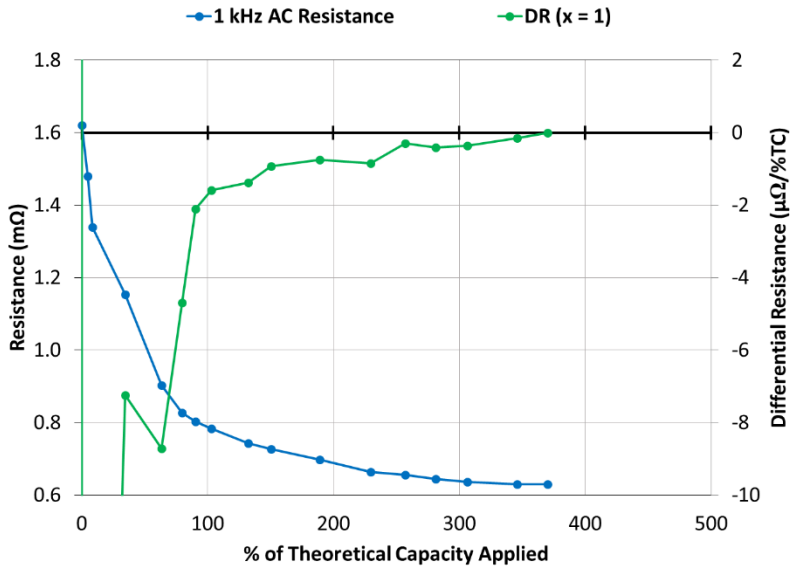
Figure 46 **Differential AC ohmic resistance as termination indicator (Cell C6)**

There is certainly potential for ohmic resistance trends to be used as a termination indicator during formation. Manual AC injection measurements could be a simple way for operators at a LAB manufacturing plant to spot-check batteries as they form and end the formation when they judge the resistance trend has slowed enough. Automated DC fast-pulsing or AC injection techniques could also be implemented in the formation charger itself, but highly sensitive equipment would likely be required to match the sensitivity of slow-response resistance trends.

4.6. Verification in Industrial Setting

As outlined in Chapter 3, a final experiment was conducted at SBCL in which two strings of 108 cells each were formed using pulses for measuring internal resistance trends throughout. One string was used for removing cells for discharge tests, while the other string was left to form uninterrupted in order to obtain reliable resistance data.

As would be expected, far less control over experimental conditions was possible in the factory than was in the laboratory. Despite the far-from-ideal test parameters, the experiment was still a partial success. Figure 47 shows the voltage of the continuous 108-cell pack during formation as well as the total pack resistance measured by the back-to-back pulsing strategy. The same general trends are shown here as those observed in the

laboratory tests, where the voltage and resistance both undergo an early dip and sharp rise, after which the resistance decays downwards. After about 300%TC however, the resistance measurements become suddenly noisy. The exact cause for this is difficult to know with confidence as many non-idealities could factor in, such as the resolution of the measurement system in the factory, the continually varying temperatures in the water bath, the relatively low number of data points collected in comparison to laboratory tests, or the existing formation algorithm that the pulsing steps had to be built into.
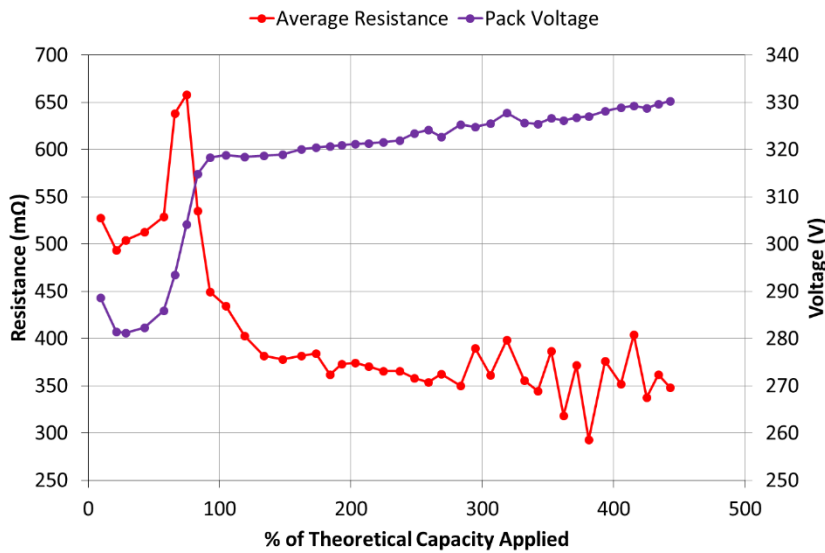
Figure 47   10-sec DC resistance and voltage of battery back formed at SBCL

The differential resistance is plotted with the discharge capacity of the cells in Figure 48. The discharge capacities follow the familiar trend of diminishing additional output with additional input, where the practical termination point would likely be around 320%TC. Due to the relatively low quality of the resistance trend shown in Figure 47, the differential resistance trend is very noisy without the filtering. Even so, the 5-point moving average applied to the $x = 4$ case still crosses the zero line near 300%TC. Thus, while the results obtained in the factory test are certainly not as clear as those obtained in the laboratory test, the proposed method for using internal resistance in detecting formation completeness has been verified for industrial scale. Considering the low level of experimenter control in this factory test, these results are promising.
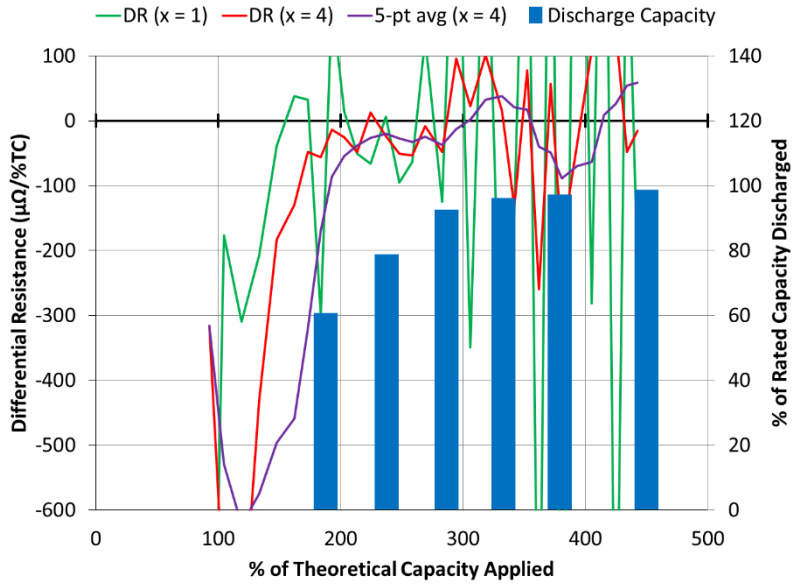
Figure 48   Termination indicator during formation at SBCL

Chapter 5   Conclusion

The main objective of this thesis is to develop internal resistance as an indicator of formation completeness in lead-acid batteries. Through extensive experimental research, this objective has been met. Lead-acid batteries were successfully formed with specifically designed pulsing strategies to evaluate the internal resistance trends as the batteries form. These trends were then correlated to the dischargeable capacity obtained during the formation. This resulted in a new research contribution which allows for formation completeness to be detected via non-invasive in situ methods using minor control changes to existing infrastructure.

From the experimental results, the following major conclusions can be drawn:

1. As a lead acid battery nears the end of formation, the measured internal resistance decays downward. This is the case for both the ohmic resistance and the kinetic resistance.

2. The more a lead-acid battery forms, the less discharge capacity output can be obtained per unit of additional formation capacity input. This trend of diminishing returns correlates with the decaying internal resistance, which can be rationalized through scientific theory regarding lead-acid batteries and general electrochemistry.

3. Both fast-response and slow-response resistances can potentially be used as termination indicators. However, slow-response resistance trends are inherently more sensitive during formation as they contain both the ohmic and kinetic responses. Furthermore, slow-response resistance trends are easier to obtain accurately since no AC waveforms or fast-logging of data are required.

4. There are many possible pulsing strategies for measuring slow-response resistance during formation (e.g. pulse up vs. pulse down, pulse magnitude, pulse duration, back-to-back pulses). Preferred techniques will have high sensitivity to accommodate the small changes that occur towards the end of formation, as well as multiple coincident measurements for averaging such as back-to-back pulsing.

78

5. Calculating the differential resistance gives rise to a numeric target representing the point at which formation should be terminated. This target is a value of zero differential resistance, approaching from the negative direction as the resistance decays downward.

6. Inherent noise when measuring small resistance change demands that averaging or filtering be applied to the differential resistance, and the resolution of the filter can shift the observed zero crossing. A tunable filter could then allow for batteries to be formed more fully when the intended end-user requires it (e.g. off-grid solar storage applications).

7. Trends observed in the laboratory were also observed in a real lead-acid battery manufacturing plant. The internal resistance method is scalable to the industrial level.

The novelty of these findings opens up additional opportunities for further research on the subject. In its present state, the study has only identified the fundamental method and some of the possibilities it holds. Extensive research is required before the identified method could be utilized on a commercial scale. With this in mind, the following recommendations are made for future research in this field:

1. Since the completed research has only focussed on container formation, the method could be tested using tank formation and circulated-electrolyte formation as well.

2. The method could also be tested in more specialized charging strategies, such as those with a mid-formation discharge or decrementing current steps at the end of formation. Combining the method with existing pulse-charge strategies would also be of interest.

3. The discharge correlation test could be repeated with very low current rates (e.g. C/100) to investigate whether the additional discharge capacity gained at high formation levels becomes more (or less) economical. These currents would be more representative of those used in off-grid solar storage applications, which would be one of the top beneficiaries of this formation method.

4. Two cell models were studied in the completed research, which differed in plate thickness but featured similar width and height. The method could be further verified through testing on much larger or smaller cells.

5. In future work, tight control over electrolyte and/or water additions during and after formation is suggested. Temperature control could also be explored in laboratory experiments through the use of a thermal chamber or a cooled water-bath system similar to that used in the factory.

References

[1] D. Berndt, "Electrochemical energy storage," in *Battery Technology Handbook*, 2nd ed., New York, NY: Marcel Dekker, 2003, pp. 1-111.

[2] D. Pavlov, "H2SO4 electrolyte - an acitive material in the lead-acid cell," in *Lead-Acid Batteries: Science and Technology*, Amsterdam, Elsevier, 2011, pp. 117-148.

[3] D. Pavlov, "Lead alloys and grids. Grid design principles," in *Lead-Acid Batteries: Science and Technology*, Amsterdam, Elsevier, 2011, pp. 149-221.

[4] M. Barak, "Lead/acid storage batteries," in *Electrochemical Power Sources*, London, Institution of Electrical Engineers, 1980, pp. 151-323.

[5] W. Boehnstedt and J. Whear, "Secondary batteries - Lead-acid systems | Separators," in *Encyclopedia of Electrochemical Power Sources*, Elsevier, 2009, pp. 620-631.

[6] S. Panero, "Electrochemical theory | Kinetics," in *Encyclopedia of Electrochemical Power Sources*, Elsevier, 2009, pp. 14-22.

[7] P. Kurzweil, "Capacitors - Electrochemical double-layer capacitors," in *Encyclopedia of Electrochemical Power Sources*, Elsevier, 2009, pp. 607-633.

[8] A. Kirchev, M. Perrin, E. Lemaire and F. Mattera, "Studies of the pulse charge of lead-acid batteries for PV applications Part I. Factors influencing the mechanism of the pulse charge of the positive plate," *Journal of Power Sources,* vol. 177, pp. 217-225, 2008.

[9] B. E. Conway, "Transition from "supercapacitor" to "battery" behavior in electrochemical energy storage," *Journal of the Electrochemical Society,* vol. 138, no. 6, pp. 1539-1548, 1991.

[10] S. Srinivasan, "Electrode/electrolyte interfaces: structure and kinetics of charge transfer," in *Fuel Cells*, New York, NY: Springer Science+Business Media, LLC, 2006, pp. 27-92.

[11] D. Pavlov, "Pastes and grid pasting," in *Lead-Acid Batteries: Science and Technology*, Amsterdam, Elsevier, 2011, pp. 253-309.

[12] D. Pavlov, "Curing of battery plates," in *Lead-Acid Batteries: Science and Technology*, Amsterdam, Elsevier, 2011, pp. 363-404.

[13] D. Pavlov and P. Nikolov, "Capacitive carbon and electrochemical lead electrode systems at the negative plates of lead-acid batteries and elementary processes on cycling," *Journal of Power Sources,* vol. 242, pp. 380-399, 2013.

[14] P. Krivik, K. Micka, P. Baca, K. Tonar and P. Toser, "Effect of additives on the performance of negative lead-acid battery electrodes during formation and partial state of charge operation," *Journal of Power Sources,* vol. 209, pp. 15-19, 2012.

[15] D. Pavlov, "Technology of formation," in *Lead-Acid Batteries: Science and Technology*, Amsterdam, Elsevier, 2011, pp. 501-531.

[16] D. Pavlov, "Formation of positive lead-acid battery plates," in *Lead-Acid Batteries: Science and Technology*, Amsterdam, Elsevier, 2011, pp. 444-479.

[17] D. Pavlov, "Processes during formation of negative battery plates," in *Lead-Acid Batteries: Science and Technology*, Amsterdam, Elsevier, 2011, pp. 481-499.

[18] D. Lambert, J. Manders, R. Nelson, K. Peters, D. Rand and M. Stevenson, "Strategies for enhancing lead–acid battery production and performance," *Journal of Power Sources,* vol. 88, pp. 130-147, 2000.

[19] M. J. Weighall, "Techniques for jar formation of valve-regulated lead-acid batteries," *Journal of Power Sources,* vol. 116, pp. 219-231, 2003.

[20] P. Senthil Kumar, K. Murthy, K. Sudarsanam and S. Vijayanand, "An exploratory study on electrolyte circulation as a means of achieving faster formation of lead acid batteries," *International Journal of Electrochemical Science,* vol. 7, pp. 1060-1070, 2012.

[21] S. C. Kim and W. H. Hong, "Fast-charging of a lead–acid cell: effect of rest period and depolarization pulse," *Journal of Power Sources,* vol. 89, pp. 93-101, 2000.

[22] F. Henn, C. Rouvet, A. de Guibert and P. Marteau, "Hydrogen and oxygen evolution in sealed lead/acid 2 V cell. In situ gas measurement by Raman spectroscopy," *Journal of Power Sources,* vol. 63, pp. 235-246, 1996.

[23] C. D'Alkaine, J. de Andrade and P. Impinnisi, "A practical method to follow the evolution of electrochemically active areas during plate formation processes in lead acid batteries," *Journal of Power Sources,* vol. 85, pp. 131-136, 2000.

[24] Y. M. Podrazhansky and B. Tsenter, "Control and termination of a battery charging process". U.S. Patent 5 694 023, 2 Dec. 1997.

[25] J. P. McKinley, S. A. Sellers and K. R. Colclazier, "Battery formation and charging system and method". U.S. Patent Application Publication 2010/0164437, 1 Jul. 2010.

[26] M. Cugnet, M. Dubarry and B. Liaw, "Secondary batteries - Lead-acid systems | Modeling," in *Encyclopedia of Electrochemical Power Sources*, Elsevier, 2009, pp. 816-828.

[27] M. Hejabi, A. Oweisi and N. Gharib, "Modeling of kinetic behavior of the lead dioxide electrode in a lead–acid battery by means of electrochemical impedance spectroscopy," *Journal of Power Sources,* vol. 158, pp. 944-948, 2006.

[28] K.-S. Ng, C.-S. Moo, Y.-P. Chen and Y.-C. Hsieh, "2nd IEEE International Conference on Power and Energy," in *State-of-charge estimation for lead-acid batteries based on dynamic open-circuit voltage*, Johor Baharu, Malaysia, 2008.

[29] K. Gandhi, "Role of electrical resistance of electrodes in modeling of discharging and charging of flooded lead-acid batteries," *Journal of Power Sources,* vol. 277, pp. 124-130, 2015.

[30] M. Thele, J. Schiffer, E. Karden, E. Surewaard and D. Sauer, "Modeling of the charge acceptance of lead–acid batteries," *Journal of Power Sources,* vol. 168, pp. 31-39, 2007.

[31] F. Huet, R. Nogueira, P. Lailler and L. Torcheux, "Investigation of the high-frequency resistance of a lead-acid battery," *Journal of Power Sources,* vol. 158, pp. 1012-1018, 2006.

[32] S. Buller, M. Thele and E. Karden, "Impedance-based non-linear dynamic battery modeling for automotive applications," *Journal of Power Sources,* vol. 113, pp. 422-430, 2003.

[33] A. Hande, "Internal battery temperature estimation using series battery resistance measurements during cold temperatures," *Journal of Power Sources,* vol. 158, pp. 1039-1046, 2006.

[34] Arbin Instruments, *MitsPro4.0 User's Manual,* Version: 4.30, Rev. 7, 6/2013.

[35] International Electrotechnical Comssion, *IEC 60896-11: Stationary lead-acid batteries - Part 11: Venten types - General requirements and methods of test,* 1st ed. ed., Geneva, 2002.

[36] T. Beckwith, R. Marangoni and J. Lienhard, Mechanical Measurement, 6th ed., Upper Saddle River, NJ: Pearson/Prentice-Hall, 2007.

[37] Fluke, *Fluke 320 and 330 Series Clamp Meters.*

[38] Fluke, *80 Series V Industrial True-RMS Multimeter with Temperature.*

[39] Omega, *Revised Thermocouple Reference Tables.*

[40] Anton Paar, *DMA 35 Portable Density/Specific Gravity/Concentration Meter.*

[41] Fluke, *Fluke 500 Series Battery Analyzers.*

Appendix A

Surrette Battery Company Cell Specifications: Cell Sets A and B

Rolls

FLOODED DEEP CYCLE BATTERIES

S-480

6 VOLTS

WEIGHT DRY:	37 kg	81	Lbs.
WEIGHT WET:	51 kg	113	Lbs.
LENGTH:	318 mm	12 1/2	Inches
WIDTH:	181 mm	7 1/8	Inches
HEIGHT:	425 mm	16 3/4	Inches

CONTAINER:	High Density Polypropylene
COVER:	High Density Polypropylene
TERMINALS:	Flag M
HANDLES:	Rope

PLATE HEIGHT:	293 mm	11.550	Inches
PLATE WIDTH:	143 mm	5.625	Inches
THICKNESS (POSITIVE):	4.32 mm	0.170	Inches
THICKNESS (NEGATIVE):	3.05 mm	0.120	Inches

Certified System™
SAI GLOBAL
ISO 9001
Quality

CELLS:	15 Plates/Cell	3	Cell
SEPARATOR THICKNESS:	2 mm	0.061	Inches
GLASS MAT INSULATION:	1 mm	0.02	Inches
ELECTROLYTE RESERVE: ABOVE PLATES	57 mm	2.25	Inches

COLD CRANK AMPS (CCA):	0°F / -17.8°C	1151
MARINE CRANK AMPS (MCA):	32°F / 0°C	1440
RESERVE CAPACITY (RC @ 25A):		814 Minutes

CAPACITY   375 AH

HOUR RATE:	SPECIFIC GRAVITY	CAPACITY / AMP HOUR	CURRENT / AMPS
@ 100 HOUR RATE	1.280	486	4.86
@ 72 HOUR RATE	1.280	459	6.38
@ 50 HOUR RATE	1.280	438	8.76
@ 24 HOUR RATE	1.280	386	16.09
@ 20 HOUR RATE	1.280	**375**	18.75
@ 15 HOUR RATE	1.280	352	23.45
@ 12 HOUR RATE	1.280	334	27.81
@ 10 HOUR RATE	1.280	319	31.88
@ 8 HOUR RATE	1.280	300	37.50
@ 6 HOUR RATE	1.280	278	46.25
@ 5 HOUR RATE	1.280	263	52.50
@ 4 HOUR RATE	1.280	244	60.94
@ 3 HOUR RATE	1.280	221	73.75
@ 2 HOUR RATE	1.280	191	95.63
@ 1 HOUR RATE	1.280	135	135.00

CYCLE LIFE VS. DEPTH OF DISCHARGE
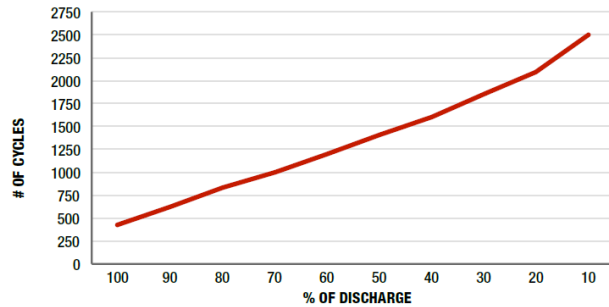
VOLTAGE VS. DEPTH OF DISCHARGE

VOLTAGE 20 HR
VOLTAGE 10 HR
VOLTAGE 3 HR
VOLTAGE 1 HR

WWW.ROLLSBATTERY.COM
SPEC 01

SURRETTE BATTERY COMPANY 1 STATION RD SPRINGHILL, NS CANADA B0M 1X0
12/1/2013   REV. 1

Rolls
BATTERY ENGINEERING
WWW.ROLLSBATTERY.COM   MADE IN CANADA

DEEP CYCLE
SERIES: 5000
MODEL: 16 CS 15 P

BATTERY TYPE: 32 VOLTS

DIMENSIONS:

LENGTH	684 MM	26 15/16	INCHES
WIDTH	686 MM	27	INCHES
HEIGHT	521 MM	20 1/2	INCHES

WEIGHTS:

WEIGHT DRY	290 KG	640 LBS.
WEIGHT WET	472 KG	1040 LBS.

CONTAINER CONSTRUCTION:

CONTAINER: (INNER)   POLYPROPYLENE
COVER: (INNER)   POLYPROPYLENE - HEAT SEALED TO INNER CONTAINER
CONTAINER: (OUTER)   HIGH DENSITY POLYETHYLENE
COVER: (OUTER)   HIGH DENSITY POLYETHYLENE SNAP FIT TO OUTER CONTAINER

TERMINALS: FLAG WITH STAINLESS STEEL NUTS AND
HANDLES: NONE

PLATES:

POSITIVE PLATE DIMENSION:

HEIGHT	273 MM	10.750 INCHES
WIDTH	143 MM	5.625 INCHES
THICKNESS	6.73 MM	0.265 INCHES

NEGATIVE PLATE DIMENSION:

HEIGHT	273 MM	10.750 INCHES
WIDTH	143 MM	5.625 INCHES
THICKNESS	4.70 MM	0.185 INCHES

CELLS: 16   **PLATES/CELL:** 15

POSITIVE PLATE DOUBLE WRAPPED WITH SLYVER ENVELOPED WITH HEAVY DUTY SEPARATOR
SEPARATOR:

THICKNESS	3 MM	0.105 INCHES

INSULATION:

GLASS MAT	1 MM	0.020 INCHES

CAPACITY:

CRANK AMPS:

COLD (CCA)	0ºF / -17.8ºC	2027
MARINE (MCA)	32ºF / 0ºC	2534

ELECTROLYTE RESERVE:

ABOVE PLATES	83 MM	3.25 INCHES

RESERVE CAPACITY:

RC @ 25A	969 MINUTES

20 HR RATE: 478

	HOUR RATE	SPECIFIC GRAVITY	CAP / AH		CURRENT / AMPS
CAPACITY @	100 HOUR RATE	1.280 SP. GR.	674	636	6.74
CAPACITY @	72 HOUR RATE	1.280 SP. GR.	636	602	8.83
CAPACITY @	50 HOUR RATE	1.280 SP. GR.	588	569	11.76
CAPACITY @	24 HOUR RATE	1.280 SP. GR.	497	492	20.7
CAPACITY @	**20 HOUR RATE**	**1.280 SP. GR.**	**478**	478	**23.9**
CAPACITY @	15 HOUR RATE	1.280 SP. GR.	445	449	29.6
CAPACITY @	12 HOUR RATE	1.280 SP. GR.	416	425	34.7
CAPACITY @	10 HOUR RATE	1.280 SP. GR.	397	406	39.7
CAPACITY @	8 HOUR RATE	1.280 SP. GR.	373	382	46.6
CAPACITY @	6 HOUR RATE	1.280 SP. GR.	339	354	56.6
CAPACITY @	5 HOUR RATE	1.280 SP. GR.	320	335	64
CAPACITY @	4 HOUR RATE	1.280 SP. GR.	296	311	74
CAPACITY @	3 HOUR RATE	1.280 SP. GR.	268	282	89
CAPACITY @	2 HOUR RATE	1.280 SP. GR.	229	244	115
CAPACITY @	1 HOUR RATE	1.280 SP. GR.	163	172	163

Surrette
BATTERY COMPANY LIMITED
ATION RD   SPRINGHILL, NOVA SCOTIA   CANADA   B0M 1X0   1.800.681.9914

REV.2
Jan-10
16 CS 15 P

Appendix B

Uncertainty Analysis

For a calculation $y = f(x_1, x_2, \ldots, x_n)$, the uncertainty, u, in y is given as [36]:

$$u_y = \sqrt{\left(\frac{\partial y}{\partial x_1} u_1\right)^2 + \left(\frac{\partial y}{\partial x_2} u_2\right)^2 + \cdots + \left(\frac{\partial y}{\partial x_n} u_n\right)^2} \tag{22}$$

Uncertainty in the experimental results of this project comes from the accuracy of the power-cycler measurements of current, voltage, and temperature, and the accuracies of the electrolyte density meter and AC injection battery analyzer. Current and voltage measurements were also verified using handheld digital meters. Table 12 lists the bias uncertainty associated with each measurement instrument.

Table 12   Bias uncertainty of measurement instruments

Measurement	Instrument	Range	Accuracy/Bias Uncertainty
Current	Power-cycler	± 100 A	0.1% of range = 0.2 A [34]
	Clamp meter	0 – 600 A	2% of value + 0.3 A [37]
Voltage	Power-cycler	0 – 20 V	0.1% of range = 0.02 V [34]
	Digital multimeter	0 – 600 V	0.05% of value [38]
Temperature	Power-cycler	N/A	Not specified
	T-type thermocouples	N/A	1.0 °C or 0.75% of value [39]
Electrolyte density	Density meter	0 – 3 g/cm^3	0.001 g/cm3 [40]
AC injection resistance	Battery analyzer	0 – 3 mΩ	1 % of value + 0.008 mΩ [41]

Firstly, uncertainty in current measurements propagate into the capacity of formation and capacity of discharge, where the capacity, *Cap,* is calculated by summing the products of each current magnitude and the duration at that current:

$$u_{Cap} = \sqrt{(t \cdot u_I)^2} = 0.2t$$

For example, cell C7 was formed at 50 A for 94 hours which amounts to 4700 ± 19 Ah, which is an uncertainty of 0.4% The 50 Ah pulsing interval will also carry 0.4% uncertainty at this formation current with 0.2 Ah of uncertainty in each interval.

For discharge capacity, uncertainty will also propagate from the temperature correction in Eq. (21) due to the uncertainty in the temperature measurement. Eq. (21) is restated here for convenience:

$$Cap_r = \frac{Cap}{1 + \lambda(T_1 - T_r)} \tag{21}$$

$$u_{Cap_r} = \sqrt{\left(\frac{u_{Cap}}{1 + 0.006(T_1 - 25)}\right)^2 + \left(\frac{-0.006 Cap \cdot u_{T_1}}{1 + 0.006(T_1 - 25)^2}\right)^2}$$

For example, cell C6 was discharged at 74 A for 3.48 hours (259 Ah), yielding $u_{Cap} = 0.70$ Ah. With an initial discharge temperature of 23.47 °C and $u_{T_1} = 1\,°C$, $Cap_r = 261 \pm 1.7$ Ah which is 0.6% uncertainty. If u_{T_1} is increased to 2 °C to account for the unspecified accuracy of the power-cycler's temperature measurements, the uncertainty increases to 1.2%, which is still very low. The uncertainty in Eq. (21) itself or in the constant λ are not specified by IEC and are therefore assumed to be negligible.

Both current and voltage will influence the uncertainty of the internal resistance calculation from Eq. (19):

$$IR_t = \frac{E_t - E_0}{I_t - I_0} \tag{19}$$

$$u_{IR_t} = \sqrt{\left(\frac{u_{E_t}}{I_t - I_0}\right)^2 + \left(\frac{-u_{E_0}}{I_t - I_0}\right)^2 + \left(\frac{-(E_t - E_0)u_{I_t}}{(I_t - I_0)^2}\right)^2 + \left(\frac{(E_t - E_0)u_{I_0}}{(I_t - I_0)^2}\right)^2}$$

For example, given $I_0 = 50.03$ A, $I_t = 80.04$ A, $E_0 = 2.7678$ V, and and $E_t = 2.8248$ V, the calculated resistance calculation is then 1.90 ± 0.94 mΩ, which is an uncertainty of 50 %. The specified voltage accuracy of the power-cycler gives rise to this large uncertainty in the resistance calculation. The sample calculation is based on the final pulsing interval of cell C6, where the voltage difference in the pulse is smallest and therefore most susceptible to this bias, but this is nonetheless unacceptable uncertainty. To improve upon

this, the power-cycler voltage measurements were calibrated against a digital multimeter with an uncertainty of only 0.05%. Voltages measured by the power-cycler were consistently verified to be equal with the highest resolution of the multimeter, which is 0.001 V. The power-cycler voltage measurements can therefore be considered calibrated such that the accuracy of the multimeter better represents the actual bias uncertainty in the power-cycler's voltage measurements. Using this improved uncertainty, the resistance calculation then equates to 1.90 ± 0.068 mΩ, which is an uncertainty of only 3.6 %. A worst-case bias uncertainty of less than 4 % is much more acceptable than the power-cycler specifications suggest. These calculations were carried out for each pulsing interval of the cell C6 formation, and the results are shown in Figure 49 with error bars representing the uncertainty at each interval.
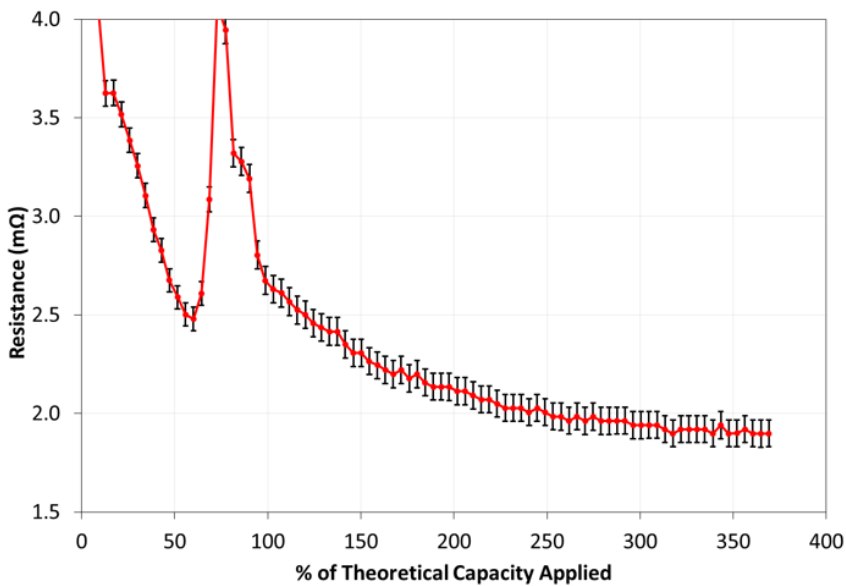

Figure 49   Cell C6 pulse resistance with error bars

An uncertainty analysis was not performed for the factory experiments, as accuracy specifications were not available for the formation system used. Calibration with handheld meters was also unfeasible as the built-in voltage measurements are taken within the structure of the formation charger.